ANALYSIS AND APPLICATION OF THE BI-DIRECTIONAL SCATTER DISTRIBUTION FUNCTION OF PHOTONIC CRYSTALS

THESIS

Robert B. Lamott, Captain, USAF

AFIT/GEO/ENP/09-M01

DEPARTMENT OF THE AIR FORCE
AIR UNIVERSITY

AIR FORCE INSTITUTE OF TECHNOLOGY

Wright-Patterson Air Force Base, Ohio

The views expressed in this thesis are those of the author and do not reflect the official policy or position of the United States Air Force, Department of Defense, or the United States Government.

AFIT/GEO/ENP/09-M01

ANALYSIS AND APPLICATION OF THE BI-DIRECTIONAL SCATTER DISTRIBUTION FUNCTION OF PHOTONIC CRYSTALS

THESIS

Presented to the Faculty

Department of Engineering Physics

Graduate School of Engineering and Management

Air Force Institute of Technology

Air University

Air Education and Training Command

In Partial Fulfillment of the Requirements for the

Degree of Master of Science in Electrical Engineering

Robert B. Lamott, BSEE

Captain, USAF

March 2009

AFIT/GEO/ENP/09-M01

ANALYSIS AND APPLICATION OF THE BI-DIRECTIONAL SCATTER DISTRIBUTION FUNCTION OF PHOTONIC CRYSTALS

Robert B. Lamott, BSEE

Captain, USAF

Approved:

Michael A. Marciniak (Chairman)	13 Mar 09 Date
Peter J. Collins (Member)	13 MAR 09 Date
Michael R. Hawks (Member)	13 MAR 09 Date

Abstract

Photonic crystals (PCs) are periodic structures built from materials with different refractive indices repeated at sub-wavelength intervals. Recently there has been significant research looking at their unusual optical characteristics, including narrow band laser protection, and zero reflectance and high absorption anomalies. Most of the research into the optical properties of PCs has concentrated only on the small range of wavelengths and angles where these effects occur. To better understand the suitability of PCs to their task, as well as their application to other purposes, it is necessary to understand where all light leaving a PC is scattered. To accomplish this, a Complete Angle Scatter Instrument (CASI) was used to analyze the scatter from three Guided Mode Resonance Filters (GMRFs) designed for laser protection at different wavelengths. In the plane of incidence, measurements of the scatter strength were made for nearly all incident and scattered angles. Additionally, reflectance data was taken out of the plane of incidence for selected incidence angles, showing the directional reflectance for the selected incident angles. This data was used to modify existing empirically based Bi-directional Scatter Distribution Functions (BSDFs), with the goal of producing a model suitable for scene generation of complex objects coated with a GMRF surface.

Acknowledgments

I would like to thank my wife for the gracious leeway she has given me to pursue my thesis over regular household chores. I would like to express my sincere appreciation to my advisor, Dr. Michael Marciniak, and the other members of my committee, Dr. Peter Collins and Lt Col Michael Hawks, for their guidance and support throughout the course of my thesis effort; Prof. Brian Cunningham of the University of Illinois, Urbana-Champlain for providing the material samples used in this research; and Mr. Dominic Maga for keeping CASI and the laboratory running smoothly. Finally, I would like to thank all of my teachers and instructors throughout my life for pushing me to challenge myself academically, and my friends and family for their support. Thank you all.

Robert B. Lamott

Table of Contents

Page

List of Figures

Figure Page

Figure Page

List of Tables

ANALYSIS AND APPLICATION OF THE BI-DIRECTIONAL SCATTER DISTRIBUTION FUNCTION OF PHOTONIC CRYSTALS

I. Introduction

In January 2005, a New Jersey man was arrested for shining a laser at an airplane over his house [1]. Although officials do not believe that he intended to harm the flight and do not suspect terrorism, the incident makes it clear that planes are vulnerable to even simple laser pointers. Considering the availability of relatively high power lasers, officials have become worried that they could be used to blind or distract pilots during take-offs and landings. While security upgrades enabled the resumption of air travel relatively quickly after Sept. 11, 2001, there would be no quick-fix if ground based lasers began affecting the safety of air travel.

The military has other concerns regarding laser protection. In addition to the possibility of personnel disabled by blinding weapons and the fear introduced by such an attack, nearly all modern military equipment uses sensitive optical sensors, which could easily be damaged or destroyed by a properly aimed laser. Satellite systems are especially vulnerable to such an attack, as there is no economically viable way of repairing them, possibly resulting in the entire satellite being made useless.

Contemporary solutions

To prevent this type of attack, some systems have a shutter to protect themselves from excessive incident light, much like the human eye's blink response. This may protect the system, but the system is still disabled as long as the shutter is closed, which is usually the goal of such an attack. A way around this is to use an optical filter on the sensor if a laser attack is detected. The problem with this solution is that this type of filter is usually broadband, and would block out much of the light of which the sensor could otherwise make use. For this reason, this is an impractical solution for spectral imagery.

Similar solutions for personnel protection lead to similar problems. Standard laser goggles are wideband, blocking much of the ambient light, yet not effective at stopping laser radiation at all wavelengths. Often they block so much ambient light that using them at night is nearly impossible, which is when the eye is dilated and most vulnerable to a laser attack. Most optic sensors, such as those on satellites, aircraft, or ground vehicles, have a small field of view, and could protect themselves from an attack with multiple optical filters available at a moment's notice. This type of system may be fairly large, but can be incorporated into new designs. Conversely, a soldier on the ground needs a small, helmet mounted system that protects from all directions, yet does not interfere with normal vision. Standard filters are not capable of meeting these needs.

Photonic Crystal Solution

Photonic crystals (PCs) are structures made from a pattern of materials with different refractive indices repeated at sub-wavelength periods. PCs can be 1-, 2-, or 3-

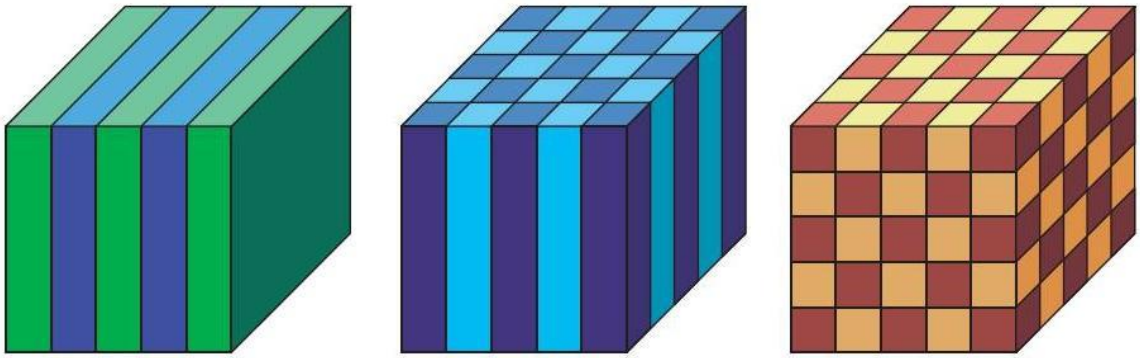

Figure 1. A visual depiction of 1-, 2-, and 3-Dimensional PCs. [2]

dimensional, depending on the number of dimensions the lattice repeats in, seen in Figure 1. The periodic structure of the lattice produces a "photonic bandgap" in much the same way that a semiconductor lattice produces an electronic bandgap. Just as a semiconductor cannot support electrons with energies in the electronic bandgap, a PC cannot support photons with optical frequencies in the photonic bandgap.

Unlike semiconductors, very few PCs have a complete bandgap. A complete bandgap would mean that bandgap wavelengths are rejected, or reflected, from every incident angle and every polarization. Most PCs behave differently for different polarizations, and they are often used in situations which limit possible incident angles. While this may limit their usefulness, new PCs are constantly being developed, and are finding their way into more and more applications [3].

PCs offer a potential solution to the problems of optical limiters, overcoming the shortcomings of ordinary optical filters, but introducing problems of their own. To overcome the wide band of a filter, a distributed Bragg reflector (DBR), a 1-D PC, can be used to protect systems against specific laser threats. DBRs are built of alternating ¼ wavelength layers of high and low index material, and are usually designed for light traveling normal to the interfaces.

While narrower than an ordinary optical filter, the reflection band of a DBR can still be tens of nanometers wide, making this system of limited use for some spectral imagery systems. Also, the band that a DBR reflects shifts as incident light moves off-normal because the interfaces are no longer ¼ λ apart. This negates any usefulness to wide Field of View (FOV) systems, like the human eye. DBRs are also generally delicate, and are most often used for static mirrors in optical equipment.

Another type of 1-D PC is a guided-mode resonance filter (GMRF). Rather than layers being stacked in the direction of light propagation like a DBR, GMRFs are similar to diffraction gratings, with a series of grooves built perpendicular to the light propagation, but on a subwavelength scale. Because of this structure, they are also referred to as surface PCs. A significant advantage of this type of structure is its ease of manufacturing compared to most PCs, which must be built individually much like an integrated circuit. Prof. Brian Cunningham of the University of Illinois, Urbana-Champlain, has demonstrated GMRFs made using a mold and UV cured polymer (UVCP), significantly reducing the time and cost required to fabricate them. This process also allows creating PCs with large areas, measuring tens of centimeters square, suitable for studying their overall reflectance and transmittance characteristics. Most PCs to date designed for optical wavelengths have been extremely small due to the high construction cost and low throughput of building PC structures individually[4], preventing this kind of analysis. For this reason, only minimal analysis of the scatter from PCs has been performed to date [5]. Without the samples provided by Prof. Cunningham using this construction method, the research presented here would not have been possible.

A cross section of a 1-D GMRF and scanning electron microscope (SEM) image of the mold used to create it are shown in Figure 2. By varying the grating period (Λ), grating height (d), center layer thickness (t), and the index of refraction for the three layers, GMRFs can be designed for nearly any wavelength. GMRFs can also be built in two surface dimensions, an example of which is shown in Figure 3. A 2-D GMRF can reduce differences in reflection due to polarization, but the analysis becomes significantly more complex.

Despite their single layer thickness, GMRFs are extremely efficient at rejecting their design wavelength. At that wavelength, only the zero- order diffraction mode is reflected due to the close spacing of the grooves. An in-depth analysis of their response to incident angle and wavelength requires rigorous coupled wave analysis (RCWA) and finite difference time domain (FDTD) analysis, often involving specialty software[6].

By changing the spacing, heights, and refractive indices of the three layers, the GMRF can be tuned to the desired frequency. Figure 4 shows how the reflectance spectra of the 2-D structure shown in Figure 3 changes as the refractive index of the

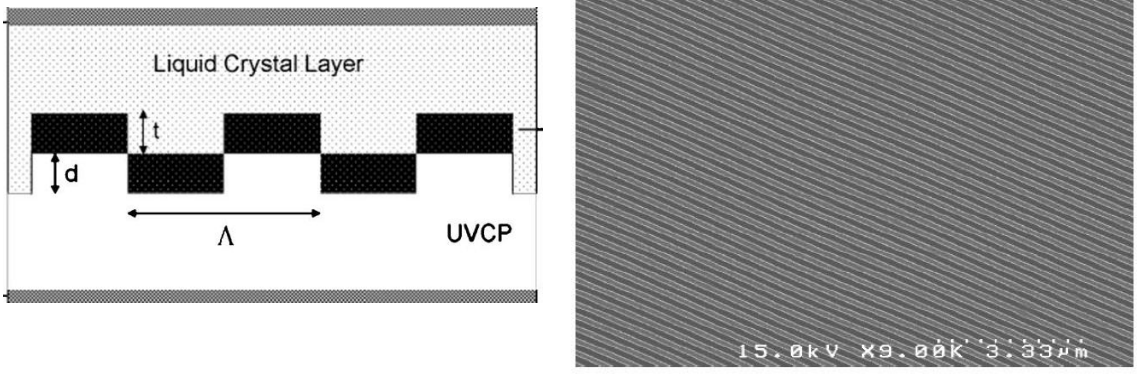

Figure 2. 1-D GMRF photonic crystal:
(left) Schematic cross section, with a liquid crystal superstrate [7]
(right) SEM image of mold used to create the GMRF [8]

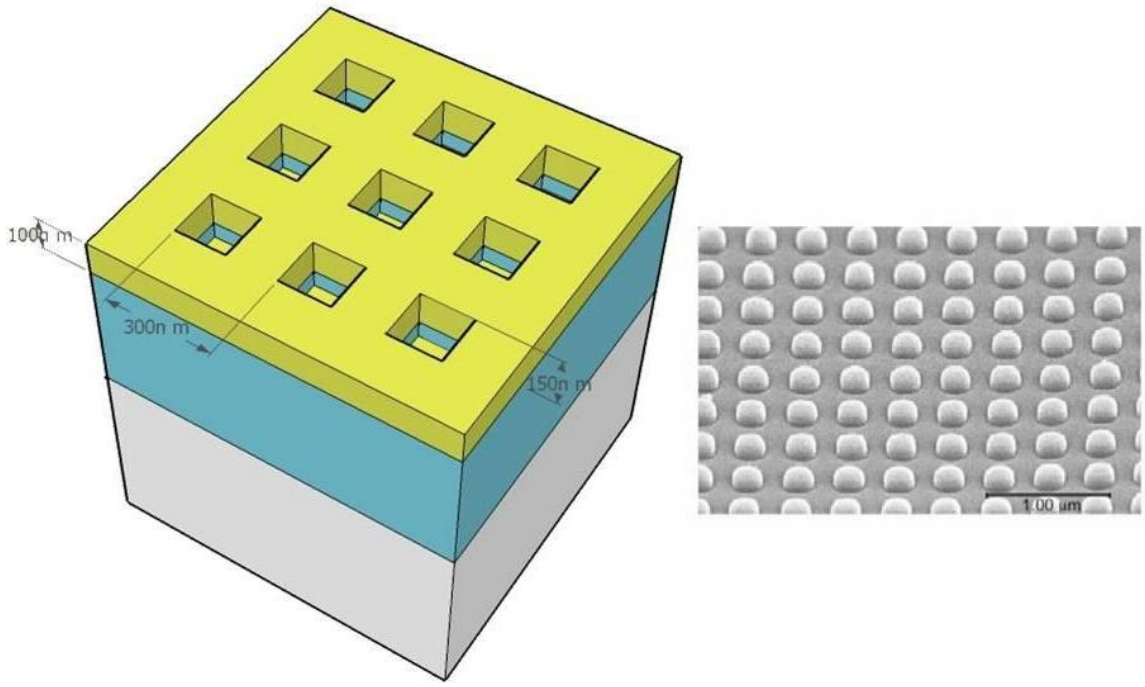

Figure 3. 2-D GMRF photonic crystal:
(left) 3-D schematic, without the superstrate[8]
(right) SEM image of the mold used to produce the PC[8]

superstrate is increased. It is important to note that this high reflectance is possible even when n=1.00, or when there is no top layer.

Additional research has shown that birefringent materials can be used as one of the layers in the GMRF structure, such as the liquid crystal superstrate in Figure 2 . The refractive index of this type of material can be changed, either electrically or optically, to cause a controlled shift in the reflectance spectra of the sample. This can allow a single layer to guard against a range of wavelengths, and to guard against tunable lasers. Because the GMRF layers are so small, multiple structures can be stacked, with each layer designed to defend against different wavelengths.

While using tunable GMRFs or other PCs for laser protection seems worthwhile, there has so far been minimal research into how it affects light except for the case of

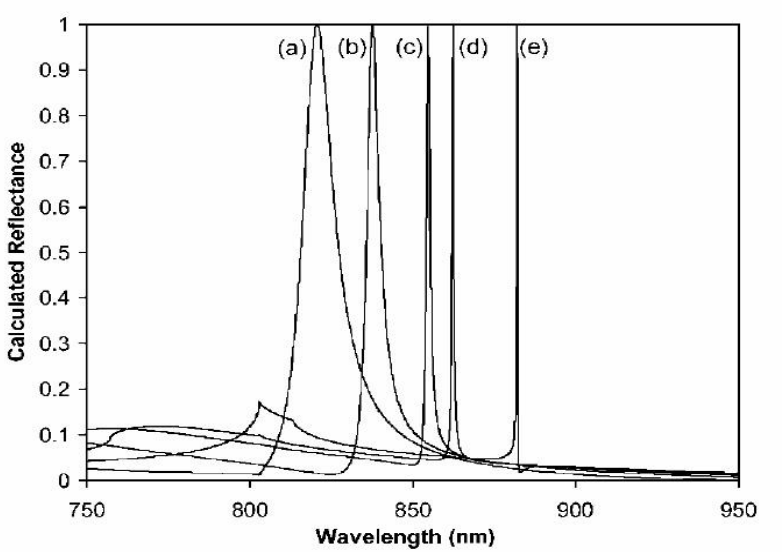

Figure 4. Calculated normal-incidence reflectance spectra with TM polarization for five different values of the superstrate refractive index: (a) 1.00, (b) 1.20, (c) 1.333, (d) 1.377, and (e) 1.479. [9]

normal incidence and transmittance. While ideally all of the light is reflected, imperfections in the PC and the finite linewidth of a laser will result in some of the light being scattered away from normal, but still in the forward direction. Without better knowledge of where the light is scattered, other problems may be introduced, such as reflecting the forward-scattered light inside the sensor housing, or directing the backward scattered towards another friendly sensor or back at the source, possibly identifying the target's location.

Application of Controlling Photonic Crystal Reflection

There has already been research in using optical and IR wavelength scale nanostructures to minimize reflection for specific incidence angles[10][11] and to modify reflection and emission spectra [12][13][14][15][16][17], as well as analyzing the scatter pattern from such materials. These show the potential of photonic crystals to decrease or redirect emitted IR energy in the first place. The coefficients of transmission, reflection,

and absorption (τ, ρ, α) denote the fraction of the incident energy which is transmitted, reflected, and absorbed at a given wavelength, and the sum of these must equal 1 at all wavelengths to conserve energy, as described by Kirchhoff's Law [18]. For a material at a given wavelength, the absorption coefficient equals its emissivity (ε), which is required to maintain thermal equilibrium [18]. These are summarized as

$$1 = \tau(\lambda) + \rho(\lambda) + \alpha(\lambda) = \tau(\lambda) + \rho(\lambda) + \varepsilon(\lambda) \quad (1)$$

This means that for opaque materials, where τ is zero,

$$\varepsilon(\lambda) = 1 - \rho(\lambda) \quad (2)$$

This shows that if a material with a high reflectance coefficient can be applied to hot surfaces which would normally emit strongly in the IR, their emission will actually be quite small despite their high temperature. A more detailed explanation of these concepts can be found elsewhere [19].

Photonic Crystal Samples and Methodology

The objective of this research is to quantitatively measure, perhaps for the first time, the forward and backward scatter off of optical PCs. However, large-area PCs are not common, typically only a few microns in size. For this research project, three prototype GMRF PC samples measuring several inches on a side were obtained from Prof. Cunningham, each designed to provide laser protection at normal incidence at a different wavelength: 532nm, 633nm, and 3.39μm. The samples are shown in Figure 5.

The 532nm sample is a 2-D structure, similar to Figure 3. It does not have a rigid mounting and is very flexible, but has plastic coatings on both sides to protect the GMRF. The 633nm and 3.39μm samples are 1-D structures, similar to Figure 2. Both are

mounted on rigid substrates, and the gratings are exposed to air, which serves as the superstrate. These open-air grooves can be seen in Figure 6.

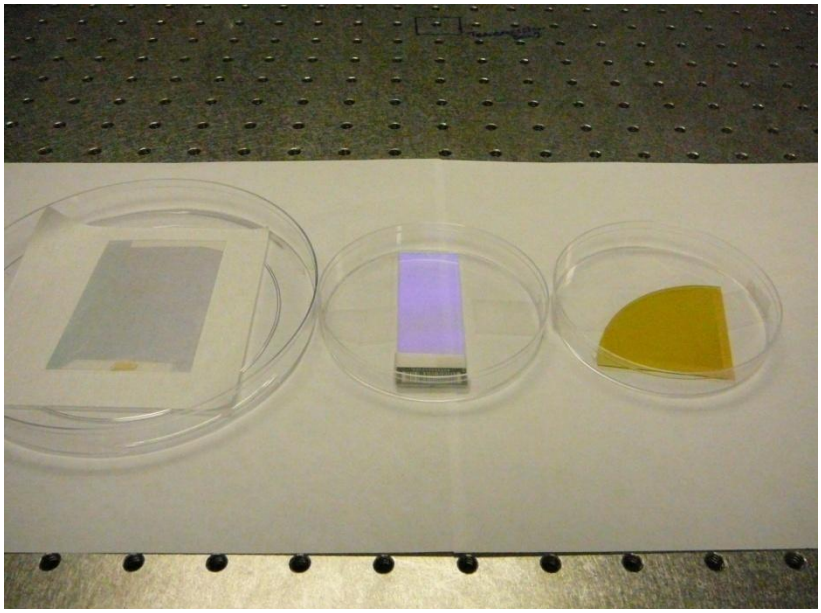

Figure 5. The three GMRF PC samples used in this experiment: (left) 2-D 532nm; (center) 1-D 644nm; (right) 1-D 3.39μm. The purple tint on the 644nm sample is diffraction from the room lights.

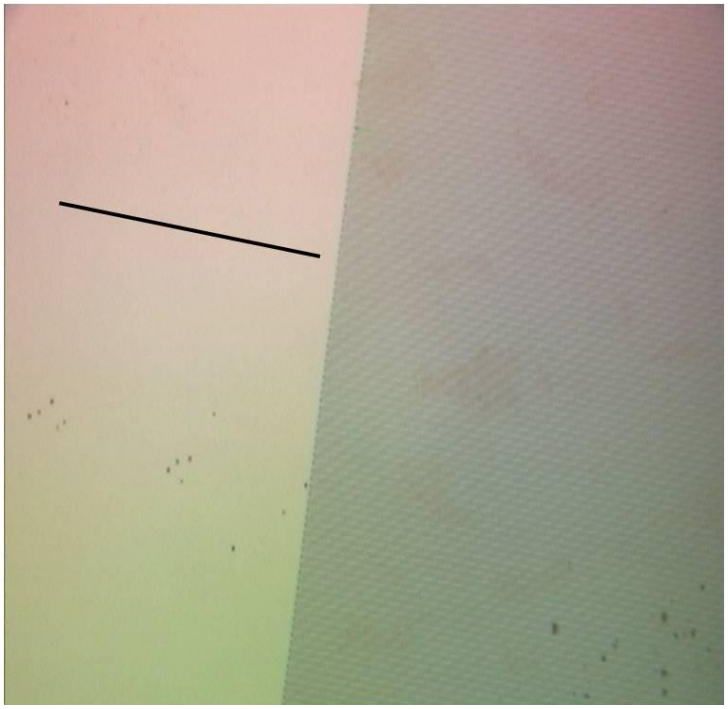

Figure 6. Microscope view of the 3.39μm sample, with the grooves visible parallel to the dark line. Other lines are due to aliasing in the camera.

The first step in understanding these materials is to analyze their spectral transmittance, which will be covered in Chapter 2. In Chapter 3, their reflectance and transmittance in the plane of incidence will be analyzed, and Chapter 4 will extend the reflectance measurements out of the plane of incidence for selected incident angles. Finally, Chapter 5 will take this data and modify an existing Bi-directional Scatter Distribution Function (BSDF) model to account for the unique scattering patterns of PCs.

II. Spectral Transmittance

Introduction

While the end goal of this research is to characterize the BSDF pattern off of a PC surface, the available BSDF collection equipment has only three laser wavelengths. Because the properties of PCs can vary strongly with wavelength, it is important to understand the spectral properties of the samples in order to recognize how the laser wavelengths relate to significant features in the spectral properties, especially minimum transmittance.

Spectral Measurements

The spectral transmittance of the samples as a function of incident angle was analyzed using a spectrophotometer for the visible samples and a Fourier Transform Infra-Red (FTIR) spectrometer for the IR sample. Reflectance was not considered at this time because the instruments would only be capable of measuring this at normal incidence, and because the BSDF collection system used later collects this data for all other incidence angles. For the 544nm sample, there were two variables tested: rotation from normal incidence, θ_i, and incident polarization, with the incident light coming in aligned with the PC structure. The other two samples have grooves in only one dimension, so the orientation of the grooves relative to the plane of incidence, ϕ_i, must also be considered. For this experiment, only parallel (ϕ_i =0°) and perpendicular (ϕ_i =90°) orientations were considered. In all three cases, only *s*- and *p*- polarizations were considered, as other linear polarizations can be made up of a combination of these two.

While additional measurements for other ϕ_i values in all samples are possible, such measurements are problematic and would not provide significant insight into the scatter distribution. Aside from being very time intensive, the angular rotation in two planes without computer control introduces significant uncertainties due to the relatively coarse scales on available rotation stages. Additionally, the spectrophotometer and FTIR have limited space available for samples, and any stage capable of rotating θ_i and ϕ_i would likely take up much of the area, and possibly block the light path for angles only slightly off of normal.

The result of these measurements is collinear transmittance $T(\theta_i, \lambda)$, where transmittance is measured over a small solid angle in the collinear direction ($\theta_t = \theta_i$), for each polarization and groove orientation, which can then be plotted in 3-D to see any trends in transmittance maxima and minima as θ_i changes. When plotting this way, one must remember that the software packages interpolate between data points, possibly showing trends that do not exist. As an alternative, a waterfall plot can be used to only plot the exact data, but this can make it difficult to read the individual incidence angles and transmittance values, and was not used.

Analysis of Spectral Transmittance Data

The full results of the spectral transmittance measurements can be found in Appendixes A-C, but a few features stand out. For the 3.39μm sample, there was no transmittance minimum at or near the design wavelength, for either polarization. To confirm this, transmittance measurements were taken using the BSDF collection system for both groove orientations and incident surfaces, which are summarized in Table 1. It

Table 1. Power transmittance of 3.39μm sample at normal incidence, incident power = 1.5mW, λ_i=3.39μm.

Groove orientation to incident polarization	Laser incident on:	Power received	%Transmittance
Parallel	Grooves	900μW	60%
Perpendicular	Grooves	750μW	50%
Parallel	Backing	810μW	54%
Perpendicular	Backing	930μW	62%

is unclear if the sample was damaged, or if it was not constructed correctly. While the grating period was known, it was not possible to model the sample because the depths and refractive indices of the layers were unknown.

For the 532nm and 633nm samples, the design wavelength at normal incidence appears to be slightly off of the actual wavelength of minimum transmittance, shown in Figures 7Figure 7 and 8. This does not affect this experiment negatively, but does show $\Delta\lambda$, the difference between the minimum transmittance wavelength and the laser wavelength, summarized in Table 2. Because the light interaction with PC structures is very wavelength dependent, these values will be important to analyzing the data from the BSDF collection system.

Table 2. Difference between minimum transmittance and laser wavelengths, $\Delta\lambda$, expressed in nanometers and as a a percentage of the laser and design wavelengths.

Design λ (nm)	Groove-polarization orientation	$\lambda_{T_{min}}$ (nm)	λ_{laser} (nm)	$\lvert\Delta\lambda\rvert$ (nm)	$\frac{\lvert\Delta\lambda\rvert}{\lambda_{laser}}$	$\frac{\lvert\Delta\lambda\rvert}{\lambda_{T_{min}}}$
532	aligned	532.5	544	11.5	2.11%	2.16%
633	perpendicular	638	633	5	0.79%	0.78%
633	perpendicular	638	544	94	17%	14%
633	parallel	559	633	74	12%	13%
633	parallel	559	544	15	2.8%	2.7%

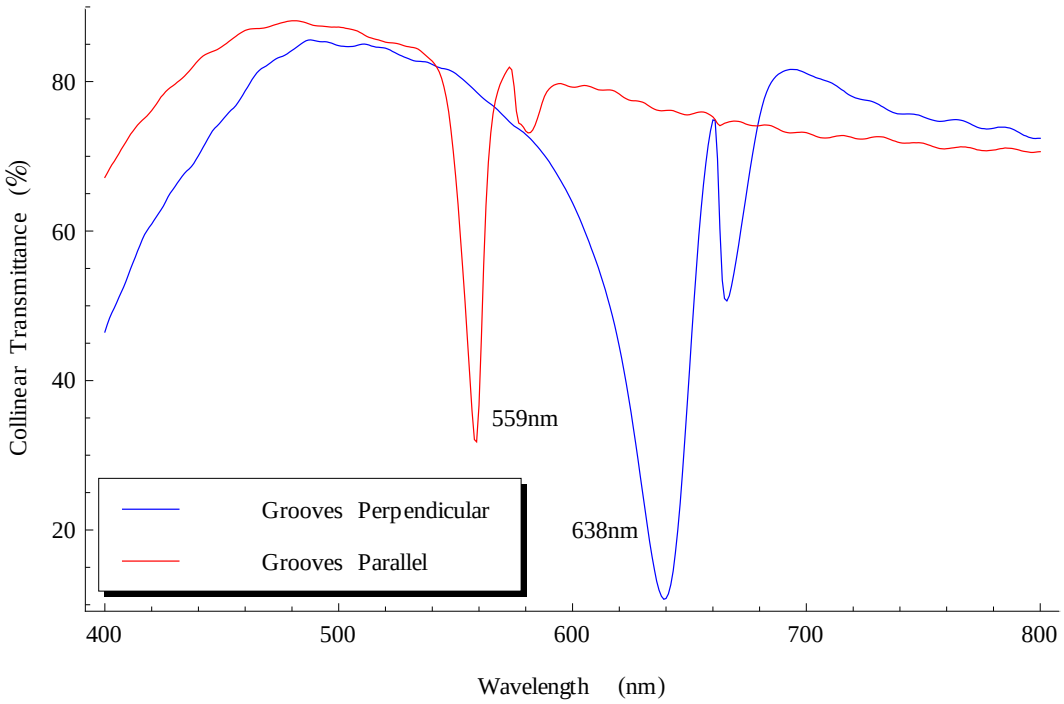

Figure 7. Transmittance spectrum of the 633nm sample at normal incidence with the grating oriented parallel and perpendicular to the incident polarization

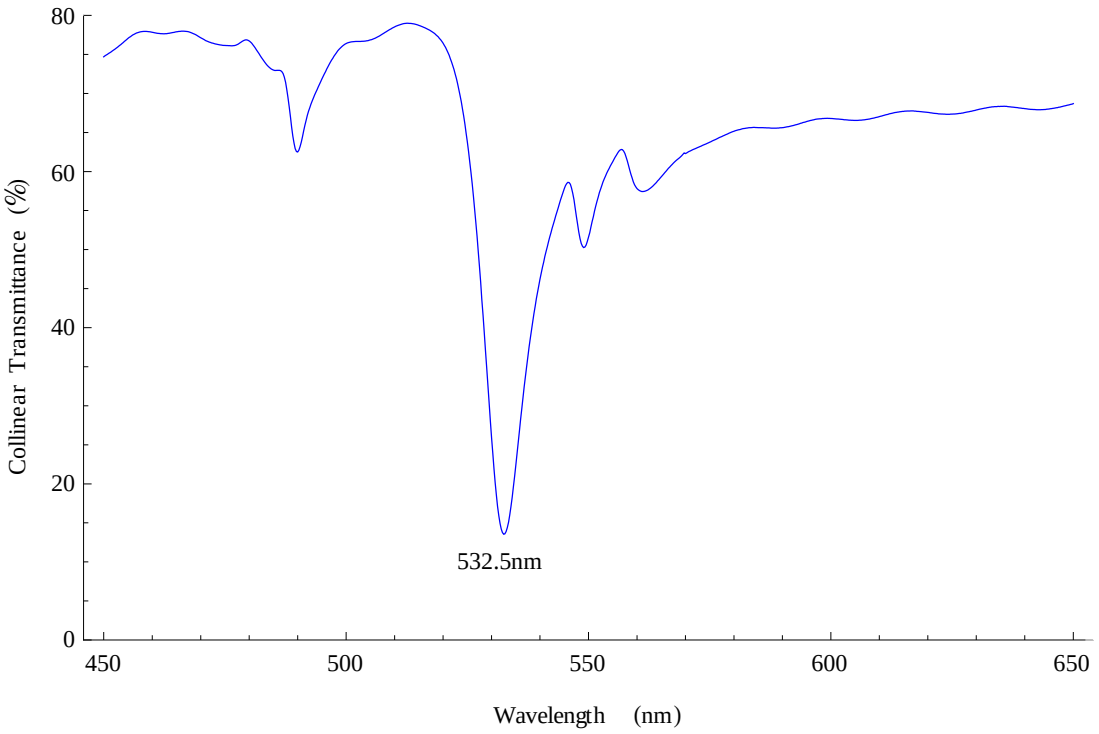

Figure 8. Transmittance spectrum of 532nm sample at normal incidence, with the polarization aligned with the PC structure.

Summary

This chapter looked at the spectral transmittance of the three photonic crystal samples studied. Because the behavior of light interacting with PC structures is very dependent on wavelength, this information, especially the $\Delta\lambda$ values, is important for extrapolating the manner in which light is scattered from these PCs at specific wavelengths to other wavelengths.

III. Scatter in the Plane of Incidence

Introduction

This chapter looks at the pattern of the light scattered by the three PC samples in the plane of incidence. Building on the previous chapter, which only looked at the collinear spectral transmittance, the measurements in this chapter look at the scatter in nearly all angles in the plane of incidence for both forward and backward scattered light, but at only specific wavelengths.

Radiometric Quantities and BSDF

To understand the scatter of a surface, a brief review of radiometric quantities is required. A more in depth explanation can be found elsewhere [18], but a summary of these quantities is shown in Table 3. The *e* subscript denotes joule units, and will be assumed for the rest of this research.

Table 3. Radiometric quantities [18]

Symbol	Quantity	Units
Q	Energy	joule
ϕ_e	Flux	watt
I_e	Intensity	watt/sr
E_e	Irradiance	watt/cm^2
M_e	Exitance	watt/cm^2
L_e	Radiance	watt/(sr cm^2)

Many of the radiometric quantities use the solid angle measurement steradian (sr). This is conceptually similar to radian measurements on a circle but extended into three dimensions on a sphere. It is the area on the surface of a sphere, divided by the squared radius of the sphere, shown in Equation (3). Although the units appear to cancel out, it is

considered its own unit, much like radians. Again, a more in-depth explanation can be found elsewhere [18].

$$\Omega = \frac{\mathrm{A}}{\mathrm{r}^2}\,[\mathrm{sr}] \tag{3}$$

A Bi-Directional Scatter Distribution Function (BSDF) is a function which describes the radiance scattered in the (θ_s, ϕ_s) direction compared to the irradiance from the (θ_i, ϕ_i) direction,

$$BSDF(\theta_s, \phi_s, \theta_i, \phi_i) = \frac{\partial L_r(\theta_s, \phi_s, \theta_i, \phi_i)\left[\frac{W}{cm^2 sr}\right]}{\partial E_i(\theta_i, \phi_i)\left[\frac{W}{cm^2}\right]} \tag{4}$$

where θ and ϕ are the elevation and azimuthal angles of a spherical coordinate system, respectively, shown in Figure 9. This can be split into a Bi-Directional Reflectance Distribution Function (BRDF) and Bi-Directional Transmittance Distribution Function (BTDF). Conceptually it is much easier to view them as separate measurements, so they will generally be treated as such.

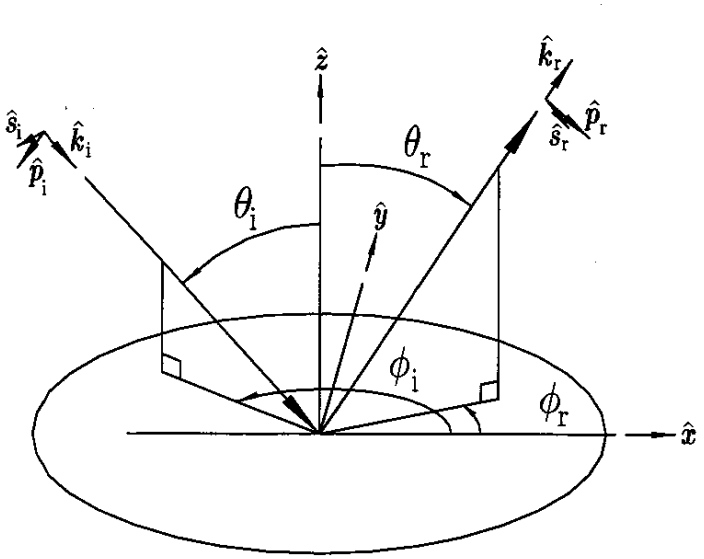

Figure 9. Geometry of a BSDF, showing θ_i, ϕ_i, θ_r, and ϕ_r, as well as the *s*- and *p*-polarization vectors and the k-vector for the incident and reflected light. [20]

BSDFs, and BRDFs in particular, are an area of active research. In the commercial world, they are heavily used in the computer graphics industry. In the DoD, they are used to generate scenes of military interest in both the visible and infrared, once a parameterized model of BRDF data has been made [21].

CASI System

The Complete Angle Scatter Instrument (CASI) system, built by Schmitt Measurement Systems, Inc., is a computer controlled, single element photodetector, which takes flux (power) measurements in an arc around a sample illuminated by a laser, and then converts this flux to a BSDF. It is able to do this because in addition to the flux, the size of the aperture and distance to the illuminated sample are known, providing the solid angle of the aperture. These measurements produce an intensity, which when divided by the incident power on the sample, provide a BSDF value. This is summarized in Equation (5).

$$BSDF = \frac{L_{detector}}{E_{sample}} = \frac{\frac{I_{det}}{A_{sample}}}{\frac{\phi_{sample}}{A_{sample}}} = \frac{I_{det}}{\phi_{samp}} = \frac{\frac{\phi_{det} \times r^2{}_{det}}{A_{det}}}{\phi_{samp}} = \frac{\phi_{det}}{\phi_{samp}\,\Omega_{det}} \tag{5}$$

In this case, A_{sample} is only the illuminated area of the sample, which assumes that the entire illuminated portion of the sample is in the FOV of the detector. There is no direct way of confirming this because the detector is only a single element, but concurrent experiments against a National Institute of Standards and Technology (NIST) certified reflectance standard have shown that the BSDF values are within 2% of the expected value when the system is aligned for the 543nm and 633nm sources, so the assumption is considered valid. The 3.39μm source achieved an error of 3%, although there is no

certified reflectance standard for comparison in the IR [22]. Even without this calibration, the error would only be a scaling error, the overall shape of the BSDF would be unchanged.

The incident flux in Equation (5), ϕ_{sample}, is determined by taking a total signal measurement, which is measured by the CASI receiver looking directly into an unobstructed beam with the widest aperture. This measurement is then scaled, as determined by the output of a photodetector inside the source box, which looks at the irradiance reflected off of a semi-reflective beam chopper, shown in Figure 10. Any variation in the output of the laser is detected by it, and the incident power is scaled by the same ratio. As a result, this scaling is transparent to the user, who is only shown the final BSDF value.

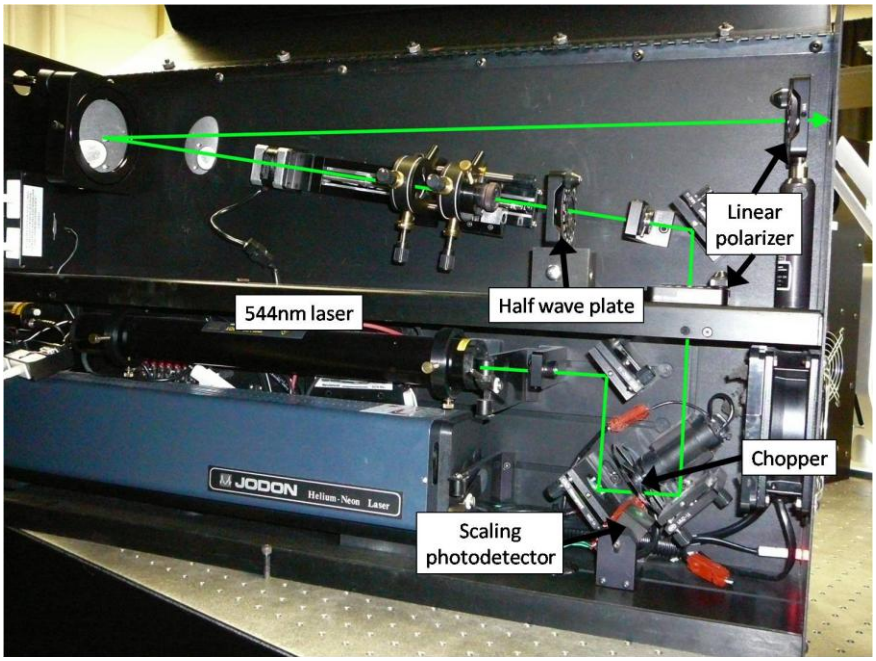

Figure 10. A CASI source box, showing the beam path, chopper, scaling photodetector, half-wave plate, and linear polarizers.

The CASI is not sensitive to ambient light, especially compared to other equipment used for collecting BRDF data. One reason for this is the chopper, which enables the CASI to take measurements of only light modulated at this frequency via lock-in detection. Additionally, the detector of the CASI views an image of a spot on the sample, so its FOV does not include significant areas of the room, and all of the detectors have chromatic filters on them to block other wavelengths from the detector.

The polarization angle of the incident and scattered light relative to the sample will not be affected by the rotation of the sample for in-plane measurements. However, the incident laser beams are not perfectly linearly polarized, and the polarization axes are not perfectly aligned either vertically or horizontally. To ensure the measurements are comparable with polarimetric data taken elsewhere, the incident polarization needs to be vertical or horizontal linear polarization. The best way to accomplish this, and ensure the largest incident power, is to use a polarizer and half-wave plate to rotate the incident polarization so that the source box emits either vertically or horizontally polarized light. For in-plane data collection, the polarization of the scattered light was not considered, but would only require adding a linear polarizer at the detector.

While up to this point polarization has only been referred to as horizontal or vertical, these are only referenced to the AFIT CASI system. Relative to the surface, the laboratory vertical polarization is equivalent to perpendicular, TE, or *s*-polarization, and the laboratory horizontal is equivalent to parallel, TM, or *p*-polarization.

As stated before, the CASI system has control over which of four apertures it uses to collect scattered light: 300μm, 1100μm, 4075μm, 13850μm. These four apertures are used to strike a balance between collection speed and signal strength on one hand, and

angular resolution on the other. This is because when measuring regular surfaces, it does not need to look for high levels of detail except near the specular peak. It then switches to wider apertures in the diffuse areas of the reflection to speed up collection time significantly, not only by taking larger steps, but also by increasing the total irradiance on the detector which allows it to detect generally weak diffuse scatter. The default setting, giving more specular detail, was used in this experiment unless data suggested a higher level of detail was needed elsewhere.

Measurements in the Plane of Incidence

The data produced by the CASI is not in a standard coordinate system: the 0° reflection point is at the specular reflection. The reason for this is evident when one considers the system was primarily designed for analyzing surface quality by taking very fine angular resolution data of the specular reflection. The CASI analysis software plots this data in log-log form, meshing positive and negative angles near a "zero" point, so that the specular piece appears very wide and the quality of the surface can be assessed very quickly without additional analysis. To convert the CASI data into standard coordinates, the rotation angle is added to the CASI angle, producing θ_r measured from normal. The resulting data is of the form (θ_r, *BRDF*) or (θ_t, *BTDF*), depending on if the measurement was reflective or transmissive, respectively. The incident angle can later be added to the each data point to produce a set of (θ_i, θ_r, *BRDF*). This entire exporting procedure is shown in Appendix D: Exporting In-Plane CASI Data.

Because the CASI is normally set to skip the portion of the reflected arc where the receiver blocks the laser, there will be a gap of approximately 8° in the reflected data at

the retro-refection angle. However, the receiver does not entirely skip the occultation, and there will usually be one data point which is several orders of magnitude lower than the other data points. If this point is not removed, it produces a line of negative peaks in a line showing the retro-reflection. Additionally, there will be an offset in the θ_r values for any collection that starts in the occultation, which also affects when the CASI switches apertures. The value of this offset will change depending on the starting point, and there is no way to switch apertures correctly. To avoid this, the starting angle measured from the surface normal should be at least 5° away from the incident angle, either higher or lower. In terms of the CASI reflected angle, this means the starting point should be 5° from $-2\theta_i$.

Plotting In-Plane Data

While the data points produced by an in-plane measurement can be used to produce a polar plot of reflection and transmission for a given incident angle, similar to Figure 11, this would require a similar plot for each incident angle, and may obscure any trends in the data.

Instead, plotting all of the (θ_i, θ_r, $log_{10}[BRDF]$) points in three Cartesian dimensions allows a single plot to show all of the data. The $\log_{10}$ of the BRDF data is used to ensure that the very strong specular peak does not overpower more subtle features, which can be over nine orders of magnitude weaker. Alternatively, it is possible to change the vertical plot limits, but this requires manual adjustment for each data set. These three alternatives are shown in Figure 12. In these plots, the incident angle is on the right, and the reflected angle is on the left. The saw tooth peak from (θ_i = 0°, θ_r = 0°)

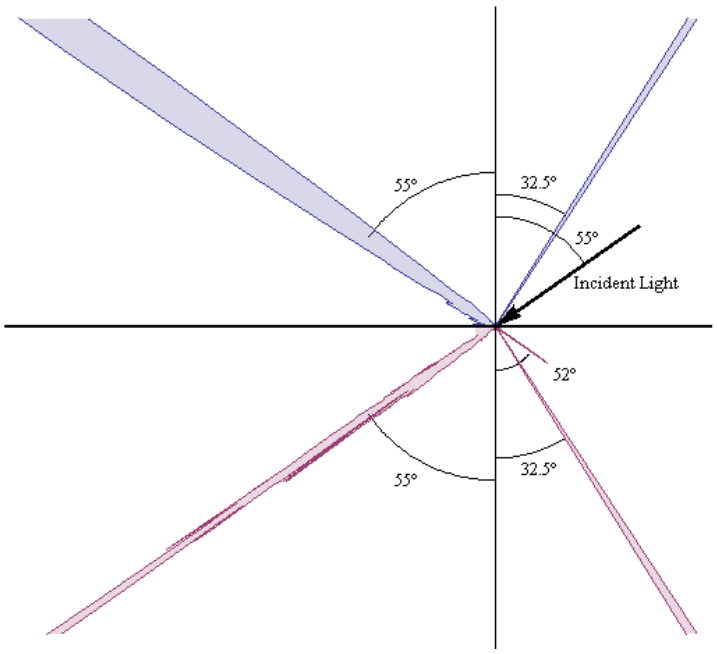

Figure 11. Polar plot of reflection (top) and transmission (bottom) of the 3.39μm sample from TM light incident at θ_i=55°, as shown by the arrow. The grating is perpendicular to the polarization.

to (θ_i = 80°, θ_r = 80°) is the specular reflection, and appears as a saw tooth due to the interpolation graphing packages used. Mirrored from this is the retro-reflection, from (θ_i = 0°, θ_r = 0°) to (θ_i = 80°, θ_r = -80°), which includes the points with a blocked incident beam. Depending on the spacing of the material, diffraction orders may appear on the plot as well, which are observed in the lower right corner of these plots. Because the grating period for PC structures is small compared to the wavelength, these diffraction patterns will usually only be the -1st order, and will appear near the retro reflection. The shape of these lines can be found by solving the diffraction equation [23],

$$d(\sin\theta_r - \sin\theta_i) = m\lambda \tag{6}$$

for θ_r as a function of θ_i for a given order, m, assuming that the structure's period, d, is known.

The 3-D plots of (θ_i, θ_r, log_{10} *[BRDF]*) and (θ_i, θ_r, log_{10} *[BTDF]*) for each sample can be found in Appendixes A-C. Generally, the reflectance data and transmittance data matched very closely.

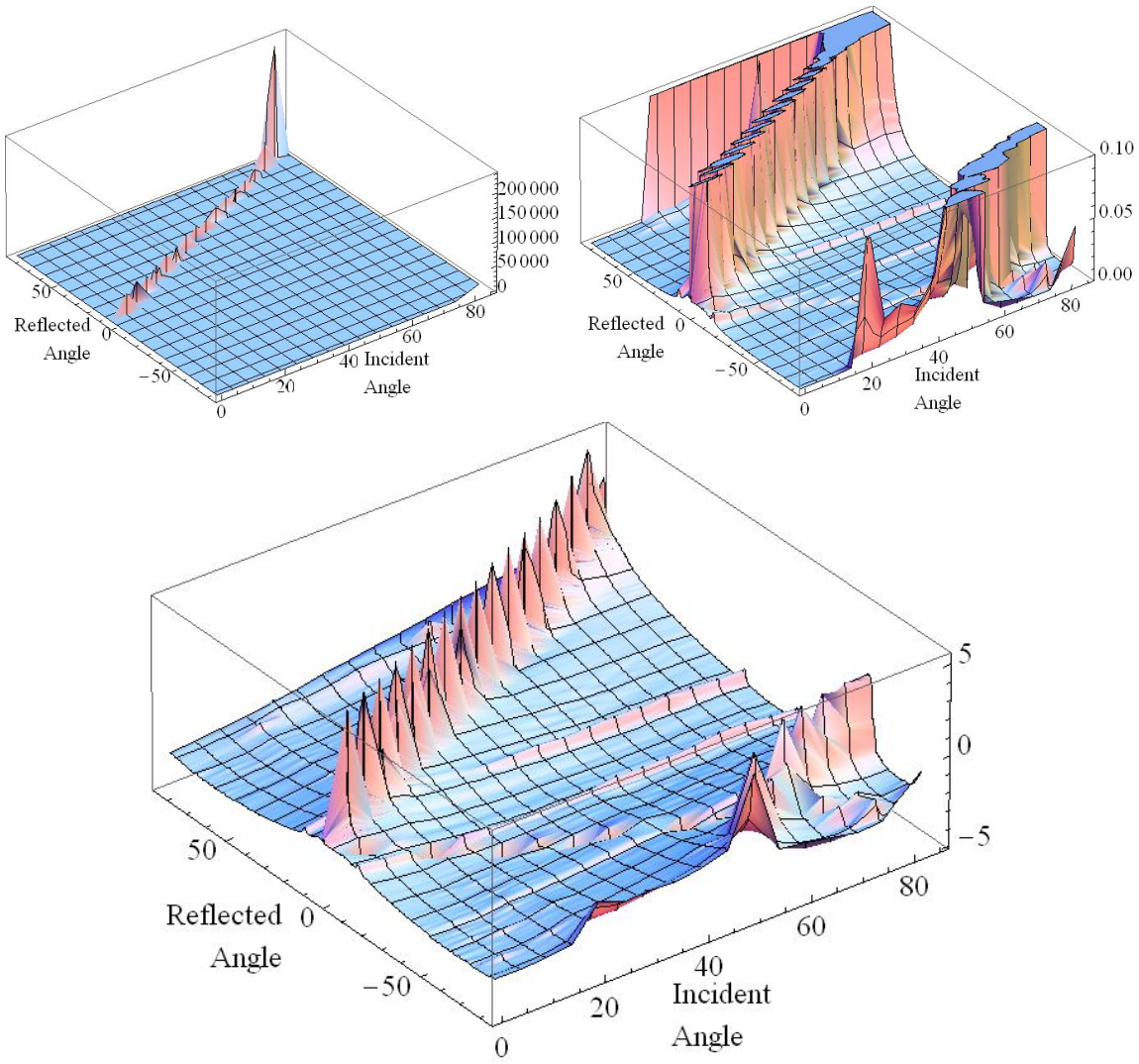

Figure 12. A comparison between a linear BRDF plot (left), a range limited BRDF plot (right), and a logarithmic BRDF plot (bottom). The logarithmic plot shows the specular reflection, the obstructed retro-reflection, a -1st order diffraction near (θ_i = 80°, θ_r = -80°), as well as peaks at constant θ_r values. This data set is from Figure 36, for *p*-polarized light with the grating perpendicular to the incident polarization

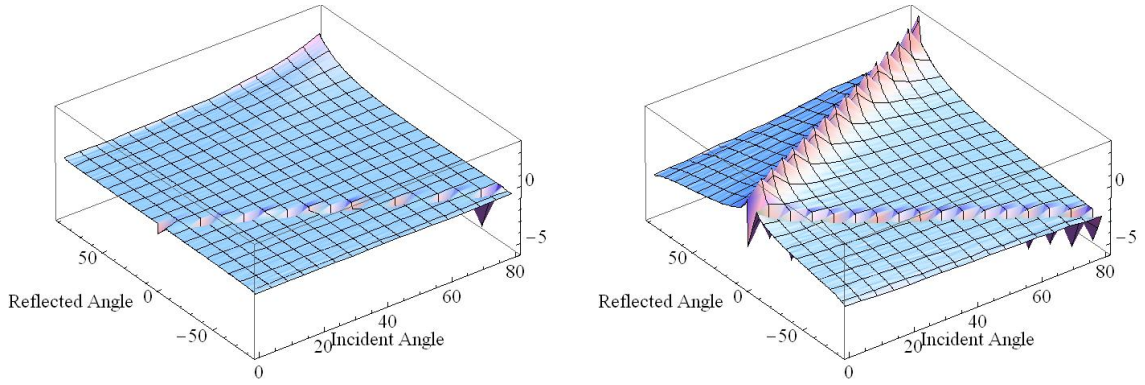

Figure 13. Log_{10}[BRDF] of white office paper (left) and aluminum foil (right) measured at 544nm, showing the specular reflection and obstructed retro-reflection, which appear as a positive ridge and a negative ridge, respectively.

Comparison with normal materials

Figure 13 shows the 3-D plots of (θ_i, θ_r, log_{10} *[BRDF]*) for two everyday materials, white printer paper and aluminum foil. Both are very reflective at the wavelength used, but the plots have significantly different shapes. The white paper is extremely flat across the entire plot, showing that it is a very diffuse surface. The peak near the top is approaching grazing incident and reflected angles, and the increased reflectance is expected for most smooth materials. The aluminum foil shows a very well defined specular ridge which is the high, mirror-like reflectance for matching incident and reflected angles. Away from this ridge, the reflectance is generally lower than for the white paper, which is expected. Both samples show a row of negative peaks, where the detector obstructed the incident beam.

Analysis of In-Plane Data

For the 544nm and 633nm data, weak peaks were seen at constant θ_i and θ_r values in Figures 27Figure 27-31Figure 31 and several subplots of 36Figure 36-39Figure 39 in Appendix A and B. For the 633nm data, the two different angles can be seen, depending

on the polarization and grating orientation. This suggests that the angle is related to the $\Delta\lambda$=5nm for *s*-polarization and $\Delta\lambda$=74nm for *p*-polarization found earlier.

A scan was then run for the θ_i value of the peaks using the smaller apertures to increase the angular resolution over the entire collection, producing Figures 14 and 15. A similar collection for the constant θ_r peak would have required individually setting up the CASI for each incident angle, and was not performed. This angle is referred to as the "resonant angle" of the PC structure at the incident wavelength because very strong constructive and destructive interference of the scattered light occurs over both the transmission and reflection hemispheres. This is observed in the spiked structures of Figures 14 and 15. While using smaller apertures allowed more detail of this structure to be captured, it is not practical to only use the smaller apertures for the entire set of (θ_i, θ_r) points. Not only would it significantly increase the collection time, but it also requires a much finer alignment of the sample. Without the sample being perfectly aligned, the scatter pattern may rotate slightly out of the plane of incidence and be missed by smaller apertures.

These patterns are also visible to the naked eye in a darkened room. Figure 16 is a photo of the reflection in an approximately 5° solid angle centered on the specular direction from the 532nm illuminated by the 544nm laser at θ_i = 25°.

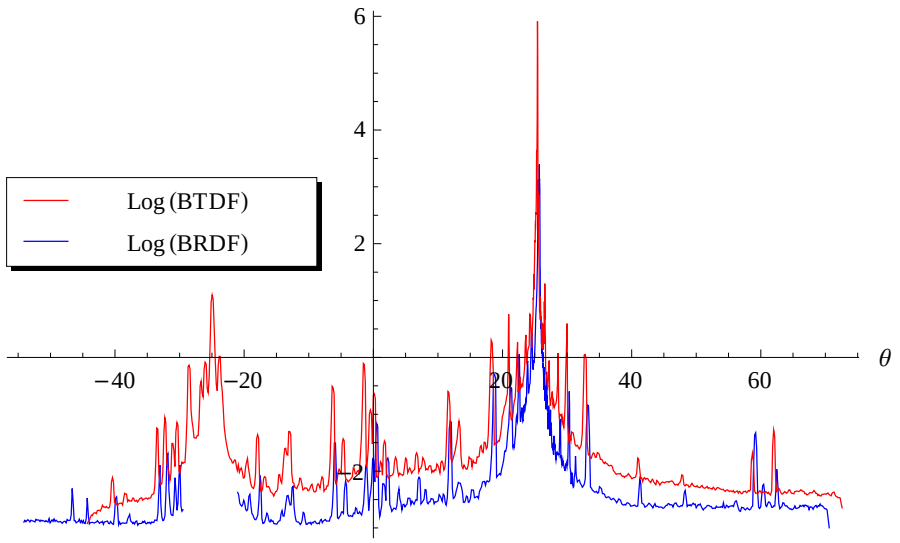

Figure 14. BRDF and BTDF of the 532nm sample measured at 544nm for θ_i=25.7°, using only the 2 smallest apertures.

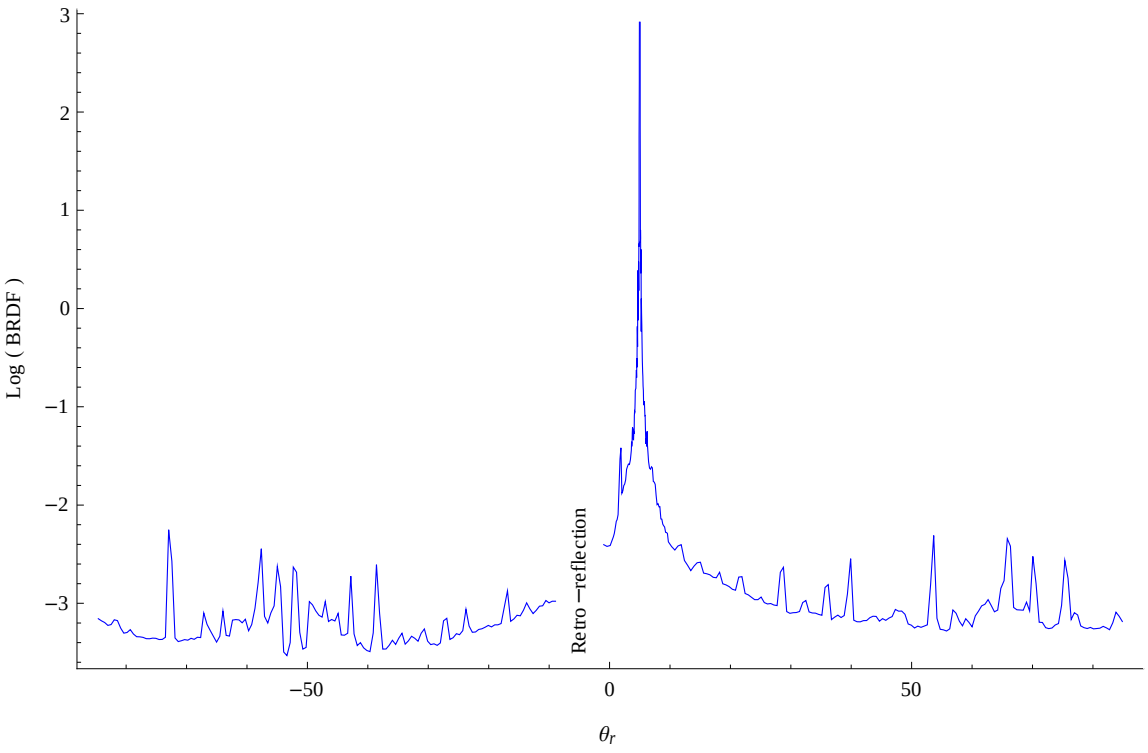

Figure 15. Plot of reflection off of 633nm sample for θ_i=5, grating parallel to polarization.

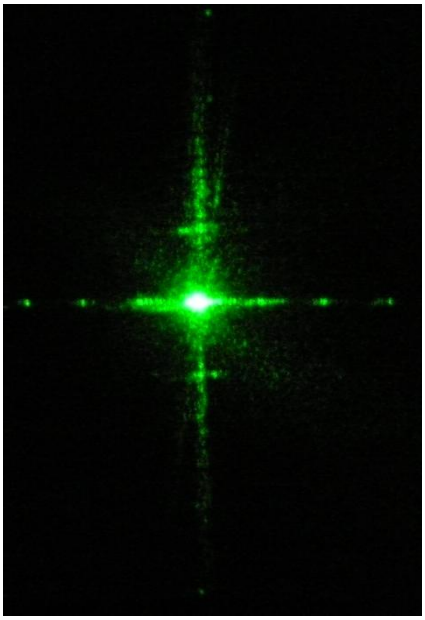

Figure 16. Photo of the pattern reflected off of the 532nm sample for θ_i = 25° near the specular direction. The central peak washed out many of the weaker features, which are easily seen with the naked eye, and can be found over much of the reflected and transmitted hemispheres.

Summary

This chapter introduced the concept of the BSDF, as well as the BRDF and BTDF. Using these concepts, it was possible to express the scatter pattern collected later in this chapter as a fraction of the incident light. "Resonant angles" appeared when the in-plane scatter was collected for two of the three PC samples. At this angle, overall scatter increased and very narrow peaks appear in the scattered light. Due to this unusual structure, the resonant angles are a worthwhile starting point for investigating the BSDF out of the plane of incidence.

IV. Measurements Out of the Plane-of-Incidence

Introduction

This chapter looks at the BRDF data out of the plane of incidence. First, it describes the required coordinate transformations needed perform out-of-plane measurements with the CASI system, which was designed for in-plane measurements. Then, it collects the out-of-plane BRDF of the 532nm sample illuminated by the 544nm laser for three different incident angles.

Coordinate System Conversion

The CASI system is designed for measurements in the plane of incidence. However, by rotating the sample about its horizontal axis, it is possible to collect BRDF data which is not in the plane of incidence. The θ_i and θ_r values produced by the CASI from a tilted sample remain laboratory centered, but the sample is no longer in agreement with this coordinate system. Because BRDF measurements need to be sample-centered, θ_i and θ_r must be transformed into this coordinate system, as must ϕ_i and ϕ_r, which are no longer constant. These are the same coordinates shown in Figure 9. Additionally, two new variables are introduced, ψ_i and ψ_r, which are the rotation of the polarization between the lab- and sample-centered coordinate systems for incident and reflected light.

For these transforms, the sample coordinate system is now defined by:

α, rotation about the vertical axis, equivalent to θ_i for in-plane data;

β, tilt about the horizontal axis (which was rotated by α);

γ, rotation of the sample about its own normal (rotated by α and β); and

δ, the location of the receiver, equivalent to θ_r for in-plane data,

which are shown in Figure 17 in both schematic form and in a photo of the CASI laboratory setup.

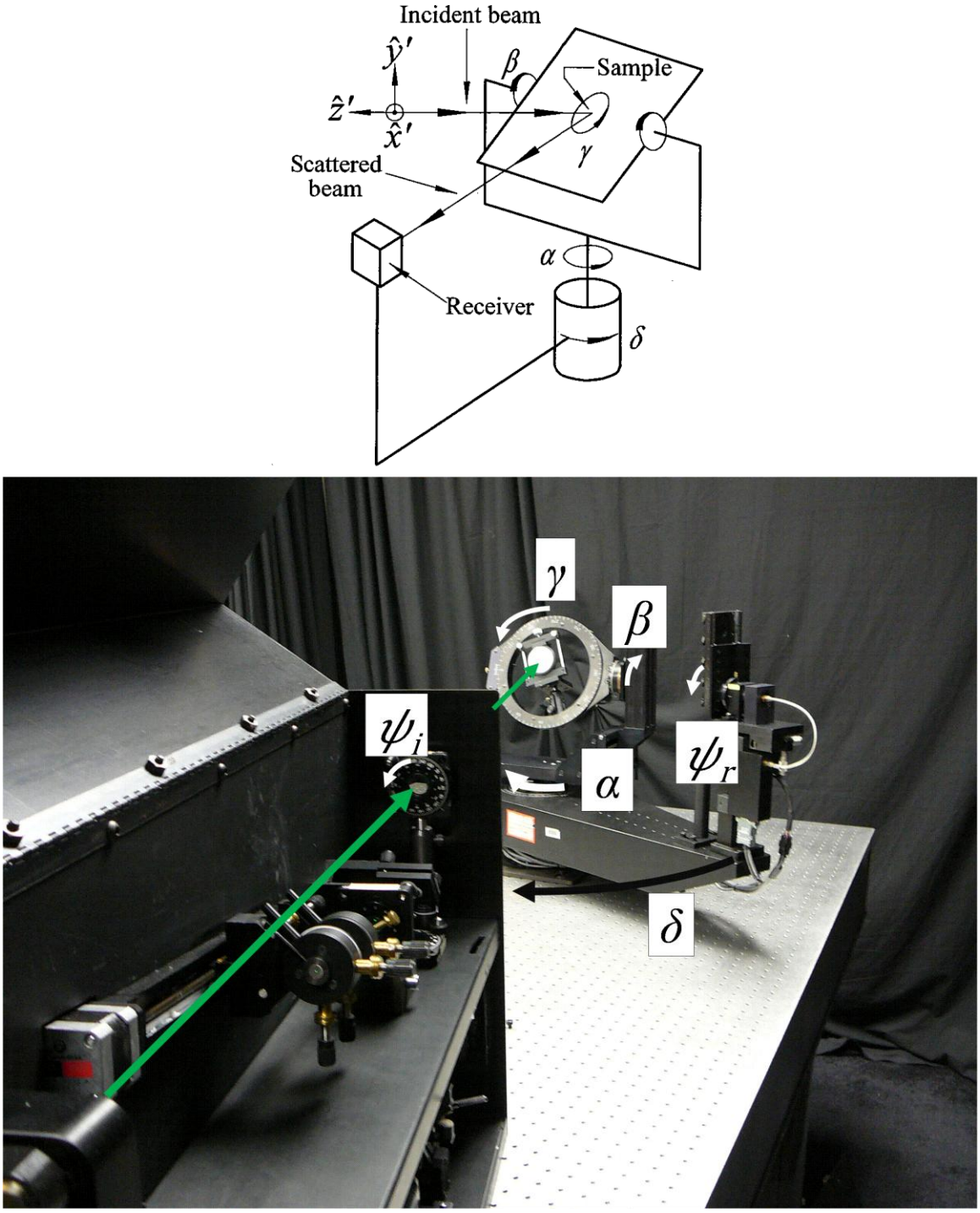

Figure 17. Schematic [20] and photo of the laboratory setup, showing angles of the sample coordinate system used for collecting out of the plane of incidence.

It is important to note that α and δ are the same as the θ_i and θ_r values reported by the CASI for all data points. It may be helpful to view the CASI as always producing α and δ values, which are equal to θ_i and θ_r for in-plane measurements. When α=β=0, the sample is normal to the incident laser; when δ=0, the receiver is blocking the laser.

The transforms between the laboratory centered and sample centered coordinates are a matter of geometry, and have been derived by Germer [20]. The transforms are:

$$\theta_i = \arccos(\cos\alpha\cos\beta) \tag{7}$$

$$\theta_r = \arccos(\cos\beta\sin\alpha\sin\delta + \cos\alpha\cos\beta\cos\delta) \tag{8}$$

$$\phi_i = \arctan\begin{pmatrix} -\cos\gamma\sin\alpha - \cos\alpha\sin\beta\sin\gamma, \\ \cos\alpha\cos\gamma\sin\beta - \sin\alpha\sin\gamma \end{pmatrix} \tag{9}$$

$$\phi_r = \arctan\begin{pmatrix} -\cos\delta\,(\cos\gamma\sin\alpha - \cos\alpha\sin\beta\sin\gamma) \\ +\sin\delta\,(\cos\alpha\cos\gamma - \sin\alpha\sin\beta\sin\gamma), \\ \sin\delta\,(\cos\gamma\sin\alpha\sin\beta + \cos\alpha\sin\gamma) \\ +\cos\delta\,(\cos\alpha\cos\gamma\sin\beta - \sin\alpha\sin\gamma) \end{pmatrix} \tag{10}$$

$$\psi_i = \arctan(-\sin\beta, \cos\beta\sin\alpha) \tag{11}$$

$$\psi_r = \arctan[\sin\beta, \cos\beta\sin(\alpha-\delta)] \tag{12}$$

In these equations, the arctan(x,y) function returns the quadrant-specific angle given by $\arctan\left(\frac{y}{x}\right)$, and is available in most mathematics software packages, including Mathematica and MatLab.

To collect 3-D BRDF data suitable for comparison to the product of BRDF models such as Sanford-Robinson, is necessary to have an incident beam from a constant θ_i direction. For anisotropic materials such as PCs, it is also necessary to hold ϕ_i and the polarization constant, relative to the material. While a set of inverse coordinate system

transforms were also developed by Germer, the data collection of the CASI makes his equations impractical for most situations. It is simpler to choose the incident beam direction(θ_i, ϕ_i) and sample rotation (α), and then solve successively for β, γ, and ψ using commonly available mathematics software, such as Mathematica or MatLab. An example of this code can be found in Appendix D. Multiple measurements will need to be taken with different α values, from $\alpha = 0°$ up to $\alpha = \theta_i$. Each of these measurements will be a "slice" through the hemisphere, with all the slices containing the incident beam.

While it does not appear that Germer's inverse transforms are necessary for out-of-plane data collection with the CASI, they are listed here for reference: [20]

$$\cos\delta = \cos\theta_i \cos\theta_r + \cos\phi_i \cos\phi_i \sin\theta_i \sin\theta_r + \sin\phi_i \sin\phi_i \cos\theta_i \cos\theta_r \tag{13}$$

$$\alpha = \arctan\left(\frac{\cos\theta_r - \cos\theta_i \cos\delta}{\cos\theta_i \sin\delta}\right) \tag{14}$$

$$\sin\beta = \frac{\sin(\phi_r - \phi_i)\sin\theta_r \sin\theta_i}{\sin\delta} \tag{15}$$

$$\gamma = \phi_i - \arctan(-\sin\alpha, \cos\alpha \sin\beta) \tag{16}$$

CASI Specific Coordinate System Transform Concerns

To correct for the incident polarization rotation, ψ_i, the incident beam needed to be rotated. It is important to note that the turning mirror in the source box induces a π phase shift in the vertical polarization, because this is the *p*-polarization relative to the mirror. This flips the polarization about the horizontal axis. While this is not an issue for in-plane measurements using pure *s*- or *p*- polarization, it is an issue for the 3-D measurements where the incident polarization must be rotated to account for ψ_i. The most straightforward solution is to place the last polarizer after the mirror inside the

source box. While this will cause a small amount of scatter off of its surface, it makes it significantly easier to visualize the correct polarizer rotation.

Once the polarizer is set to the correct angle, a half-wave plate was rotated to maximize the power leaving the final polarizer. To find this position, it was easiest to use the CASI as a photodetector, and the wave plate was rotated until the detector received maximum power. This also put the CASI detector into the proper position to collect total signal. To avoid disturbing the setup, it was best to use the horizontal adjustment to slide the sample stage out of the way, counting the number of turns required to make a clear path to the detector. Once the wave plate had been rotated correctly and the total signal collected, the horizontal stage adjustment was rotated the same number of turns in the opposite direction. While returning it to the same position is not vital if it is being moved to a new position, it was easiest to perform multiple polarization measurement (*s*-, *p*-) with the sample angle, then move on to another sample angle.

To collect the total signal, the CASI must be set to collect a signature scan, otherwise it will not move to the proper location. It is necessary to perform this step because whenever the polarization is rotated, there will be a difference in the new power. Unless the new power is collected, the BRDF measurements for the new run will use the old and incorrect Total Signal. This will only produce a scaling error in the data, and while it could be rescaled to the correct value by comparing the old and new total signal after a run is performed, this introduces a potentially large source of error. Collecting a new total signal for each polarization change is the easiest way to avoid this error.

It is also important to note that the sample mount is most likely not perfectly perpendicular to the incident beam, care needs to be taken to ensure the sample is

positioned correctly based on β and γ calculations. For a given α, the sample should first be rotated to the new γ value, then the tilt and rotation of the mount should be adjusted to have the incident beam return back onto itself, ensuring it is normal to the incident beam. The sample is now at the $\alpha = \beta = 0°$ position. The α rotation stage should be locked down as with an in-plane measurement, and the sample tilted back to the correct β angle.

Unlike ψ_i, which is only a function of α and β, the rotation of the receiver polarization, ψ_r, is a function of α, β, and the receiver position, δ. A the time of this research, the CASI system did not have the ability to control the rotation of a polarizer at the receiver.

Plotting Out-of-Plane Data

Once the out-of-plane data is collected, it must be plotted, which is done most easily using a series of coordinate rotations. First, export the data as normal, which for an in-plane measurement gives (θ_i, θ_r, BRDF). Then, plot this data in the x-z plane in 3-D Cartesian coordinates. In most cases, a logarithmic plot is needed to see reflectance features other than the specular peak. Because many of the other reflectance features are relatively weak, an offset is required in the logarithmic scale to produce positive values. Otherwise, the reflectance will appear to be in the wrong hemisphere. This produces a set of (x_1, y_1, z_1) values:

$$\begin{aligned} x_1 &= (\text{offset} + \log[\text{BRDF}]) \sin\theta_r \\ y_1 &= 0 \\ z_1 &= (\text{offset} + \log[\text{BRDF}]) \cos\theta_r \end{aligned} \tag{17}$$

Next, this data is rotated forward around the x-axis by β degrees, producing intermediate values of (x_2, y_2, z_2) data:

$$\begin{aligned} x_2 &= x_1 \\ y_2 &= y_1 \cos\beta - z_1 \sin\beta \\ z_2 &= y_1 \sin\beta + z_1 \cos\beta \end{aligned} \tag{18}$$

Finally, the data is rotated about the z-axis by γ degrees, resulting in (x_3, y_3, z_3):

$$\begin{aligned} x_3 &= x_2 \cos\gamma - y_2 \sin\gamma \\ y_3 &= x_2 \sin\gamma + y_2 \cos\gamma \\ z_3 &= z_2 \end{aligned} \tag{19}$$

When taken together, these slices only produce two opposite quarters of the hemisphere, as seen in Figure 18.

If ϕ_i was in a direction where the PC structure is symmetric about the plane of incidence, such as parallel or perpendicular to the grooves of the 1-D structure, it can be assumed that the BRDF will be symmetric about the plane of incidence, as well. In the above example, this simply means the data is mirrored about the y-z axis,

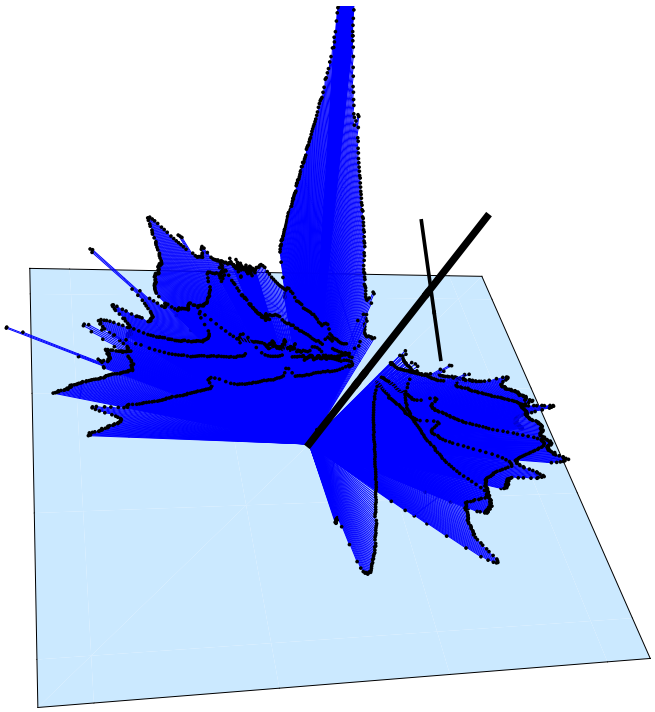

Figure 18. Out-of-plane reflectance data before mirroring. The blue lines with black tips are the BRDF data. The black line at the intersection of these lines shows the direction of the incident beam, and the smaller line perpendicular to it represents the incident polarization. The light blue square represents the PC surface.

$$\begin{aligned} x'_3 &= -x_3 \\ y'_3 &= y_3 \\ z'_3 &= z_3 \end{aligned} \tag{20}$$

However, if the PC structure is not symmetric about the plane of incidence, mirroring the data will not provide accurate results. Instead, additional data will need to be collected with new values for the sample position and polarization, as shown in Equation (21). New collections for $\beta = 0°$ and $\alpha = 0°$ are not needed, as these cases are parallel or perpendicular to the plane of incidence.

$$\begin{aligned} \alpha' &= \alpha \\ \beta' &= -\beta \\ \gamma' &= 180° - \gamma \\ \psi_i' &= 180° - \psi_i \\ \psi_r' &= 180° - \psi_r \end{aligned} \tag{21}$$

When these steps are performed for all slices of a sample, it produces a 3-D logarithmic reflectance plot with the y-z plane as the plane of incidence. For each slice, the gap in the data caused by the receiver occultation should be in this plane at θ_i degrees from normal. To provide perspective on the reflection, a line showing the incident beam is added, as well as a line representing the polarization of the incident beam. The polarization line can also help to provide a reference between plots, if it is placed at the same distance from the origin. A polygon is added to represent the PC plane, which helps with visualizing the reflected angle. Mathematica code for this entire process is shown in Appendix D.

532nm Out-of-Plane Results

This procedure was followed for the 532nm sample measured at 544nm for θ_i values of 15°, 25°, and 35° to see if the ridges at a constant θ_i and θ_r would be seen in 3-

D. The 532nm sample was selected because it is a 2-D structure, and it was expected that there would be more detail over the hemisphere than with the 633nm sample. The 3.39μm sample was not used because no peaks were seen in the in-plane data. The results, shown in Figure 19, do show the increased reflectance for the $\theta_i = 25°$, *s*-polarized case.

Summary

This chapter showed how a series of coordinate transformations and rotations can be used to obtain BSDF data out of the plane of incidence using a system designed primarily for in-plane collection. Then, out-of-plane BRDF data was collected for one of the samples at several incident angles, including the resonant angle. This is possibly the first time that out-of-plane *quantitative* scatter measurements have been made of a PC structure. (*Qualitative* out-of-plane scatter measurements focusing on the angle of peak scatter from a PC structure have recently been published by Wu, Li, and Fuh. [5])

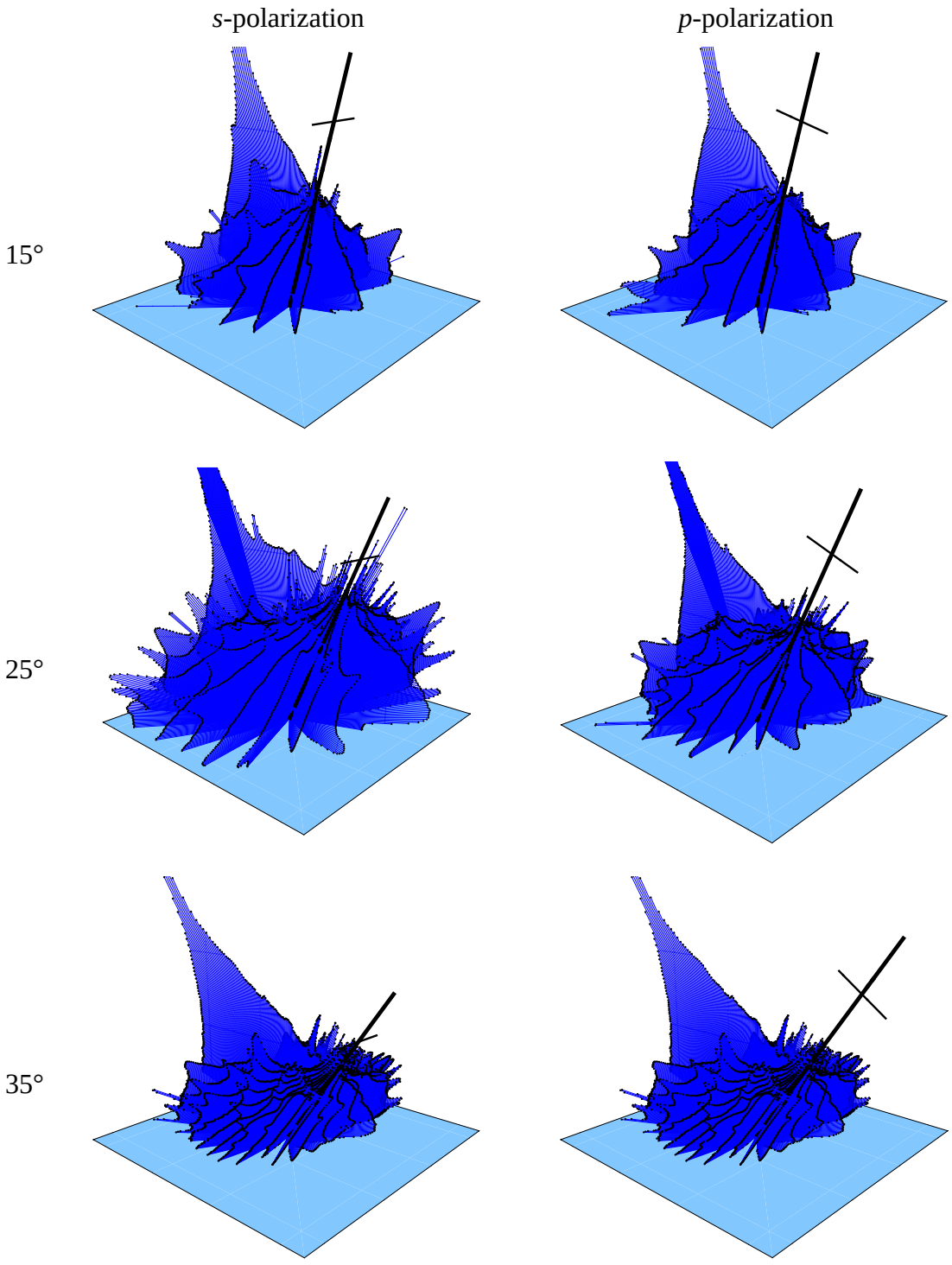

Figure 19. Plots of BRDF out of the plane of incidence for θ_i = 15°, 25°, and 35°, for *s*- and *p*-polarizations. All plots are on the same log scale.

V. Model Development

Introduction

While knowing the actual BRDF pattern of a PC structure through measurement is important, it may not be very useful in scene-generating models. Rather than using the data as a database to determine the scatter strength in each direction, it is significantly more computationally efficient to generate a model based on the data, and use the model for generating scenes. This chapter investigates using physical and empirical models for this purpose, and attempts to apply the data from the previous chapters to an existing BRDF model suitable for scene rendering.

Physical Model Development

Initially, attempts were made to analytically model the PC structures, and predict the resultant scatter pattern, using the COMSOL RF software package, which solves Maxwell's equations for a given geometry. In general, the software only models a 2-D slice of the structure, with the plane of incidence containing the surface normal. While this may have been able to provide valid in-plane models, it proved impractical.

COMSOL's RF package is primarily used to solve scenarios involving long wavelengths, relative to the structure size. When solving, it breaks homogeneous areas into a mesh, with individual mesh sections smaller than one wavelength. The structure of the PC is not homogeneous and is itself close to a wavelength, and the illuminated area is very large relative to a wavelength. These factors resulted in too many data points for the software to analyze, causing the system to either crash or give obviously erroneous results. While modeling of only a few periods of the PC can be effectively performed

with this software, the result does not translate to a large area of the PC, much like modeling a single element of a diffraction grating would not correctly model the whole.

The only case where the COMSOL RF package proved effective was for the case of normal incidence. This worked because it allowed the size of the model to be decreased significantly. However, this also prevented the model from showing scatter in other directions, and was only able to show that the transmitted beam is attenuated at the sample's design frequency. This is similar to the technique used by Prof. Cunningham to design the materials in the first place. [24]

Another issue with predictive physical modeling is it is always time intensive. Even for the simplest case of normal incidence, the software took several minutes to produce accurate results. While this may be sufficient for designing a new material for a specific application, it is impractical for modeling even in-plane reflection data for multiple incident angles. These long computation times are not acceptable for scene rendering applications, such as computer graphics or IR scene generation. In these cases a simpler and more computationally efficient model is needed.

Empirical Model Development: Sandford-Robinson Model

Empirical models have several advantages over physical models. Rather than being based on the physical structure of the material and attempting to predictively calculate the resultant BRDF, empirical models take the measured BRDF data and fit a *relatively* simple function to it. The relative simplicity of the model allows it to be used for scene rendering applications, where the reflection off of multiple surfaces with different (θ_i, ϕ_i, θ_r, ϕ_r) values need to calculated quickly, sometimes even in real-time.

While these models are never as rigorous as a physical model, and all have known issues, they are considerably faster. Of the different empirical models available, the Sandford-Robinson model was used as the basis, as it uses parameters based on physical properties of the material, rather than just fitting the data. It is also used in IR scene rendering software packages used by the DoD. Other IR applications of PC structures have already been shown[10][11]. An in depth description of the Sandford-Robinson model can be found elsewhere [25], but in simple terms, the Sandford-Robinson model breaks a reflection into a diffuse term and a specular term, with the complete model in the form $f_r(\rho_d, \varepsilon_0, b, e)$, where ρ_d is the diffuse reflectance, ε_0 is the emissivity, and b is the grazing angle reflectivity, and e is the angular width of the specular lobe, respectively. Examples of the Sandford-Robinson BRDF model for relatively specular and relatively diffuse surfaces can be seen in Figure 20**.**

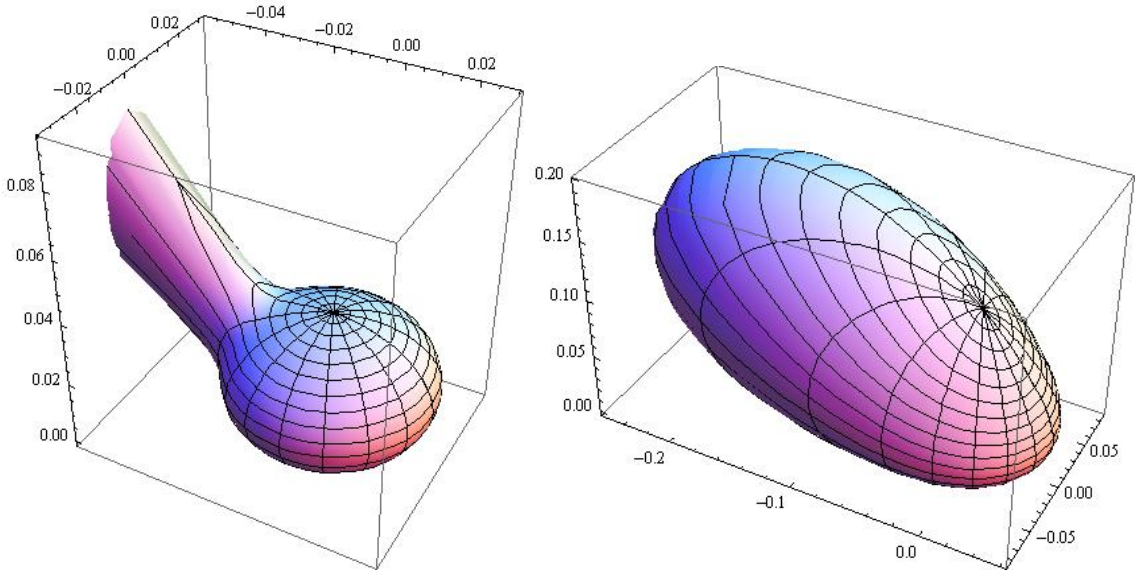

Figure 20. Examples of Sandford-Robinson BRDF models:
(left) A more specular surface
(right) A more diffuse surface

Modeling data in the plane of incidence

Once in-plane data had been collected, it was possible to develop an empirical model. While Sandford-Robinson was used as the basis, it did have to be altered significantly to model some of the unusual aspects of the PC structure.

In the 532nm and 633nm structures, there are multiple ridges with relatively strong reflections that occur at constant θ_i and θ_r values. Additionally, these values move farther from normal as the laser wavelength moves farther from the design wavelength. Because of the quick die off on either side and the general bell shape, a Gaussian function was used for these ridges. Three Gaussians were used to produce the main ridges, each of the form

$$R(\theta) = a\, e^{-\frac{(\theta - b(\Delta\lambda))^2}{2c}} \tag{22}$$

where θ is either θ_i or θ_r, a is the strength of the ridge, c is related to the width of the ridge, and b is a function of $\Delta\lambda$, and equals the resonant angle for the given $\Delta\lambda$. Due to the limited number of $\Delta\lambda$ values possible with the CASI system, b is treated as a constant for this effort. For similar reasons, b and c are also treated as constants, although there is no reason any of them must be, and collecting more data may show that they are functions of θ_i, ϕ_i, θ_r, ϕ_r, or $\Delta\lambda$, and they may have different values for different ridges.

To produce the three ridges, Gaussian functions with values of $a = 0.01\ sr^{-1}$, $b = 0.03°$, and $c = (0.0316\ °)^2$ were added to a standard Sandford-Robinson model with the parameters $\rho_d = 0.01$, $\varepsilon_0 = 0.25$, $b = 3$, and $e = 0.001$, denoted here by $f_r(\rho_d, \varepsilon_0, b, e)$. The resulting equation is then

$$BRDF = f_r(\rho_d, \varepsilon_0, b, e) + R(\theta_i) + R(-\theta_i) + R(\theta_r), \tag{23}$$

which produces the plot seen in Figure 21, which compares well to the general shape of the BRDF data containing these ridges in Appendixes A and B, although the magnitudes and ridge size and location need to be adjusted individually.

Assuming both ridges are equal, the peak created at their intersection can be removed by adding an additional term to the BRDF equation. For simplicity, this will be combined into a single R_{total} equation with the original three ridge functions,

$$R_{total} = \cdots - \frac{R(\theta_i)\,R(\theta_r)}{a^2}\frac{R(\theta_i)+R(\theta_r)}{2} \tag{24}$$

The resultant BRDF model is then seen in Figure 22. This does not model the more complex features seen in the θ_i ridge, but does compare favorably to the data gathered with a large aperture.

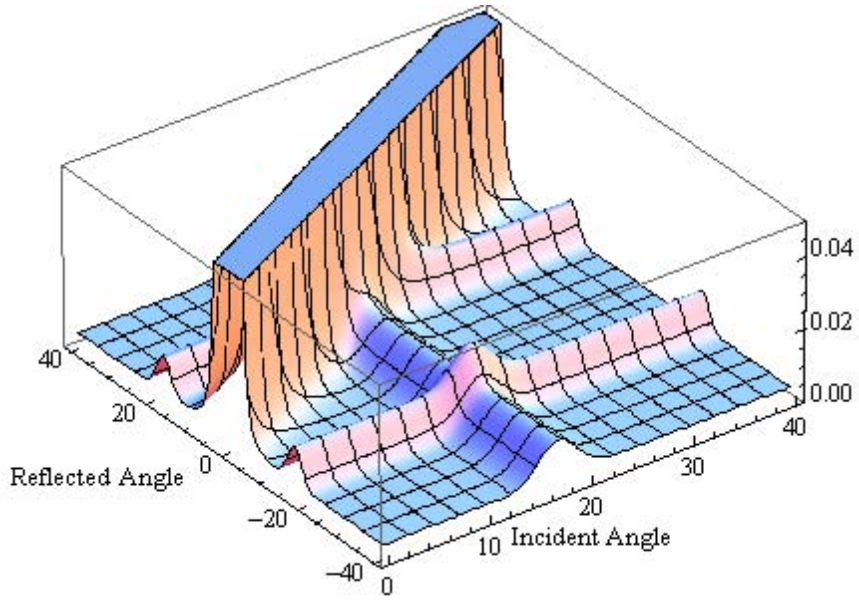

Figure 21. Model of a PC BRDF, showing the ridges at constant θ_i and θ_r.

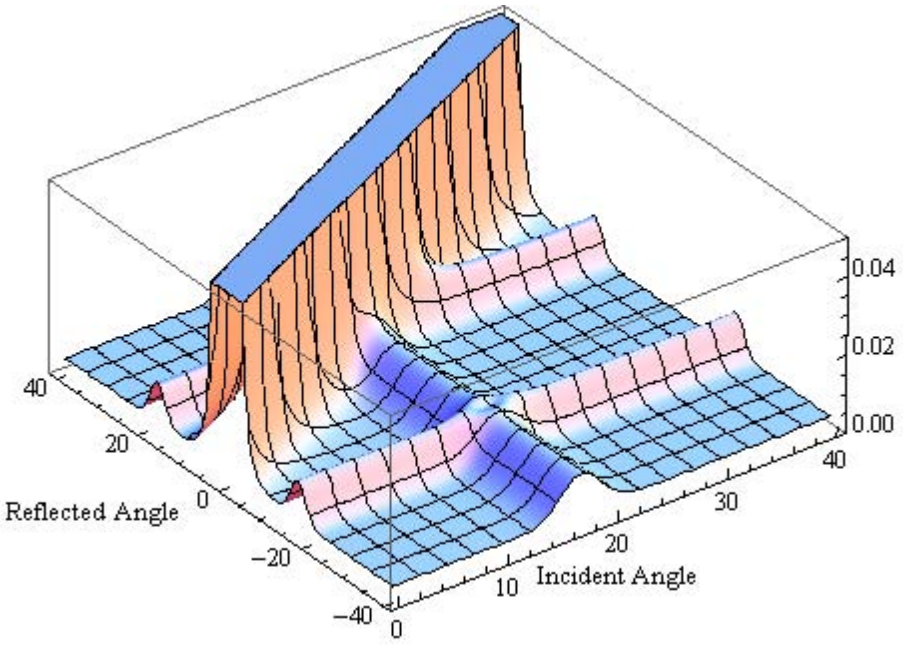

Figure 22. Model of a PC BRDF, with double ridge removed.

Modeling the diffraction modes of the PC structures for in-plane data is not difficult; it only requires solving the diffraction equation, Equation (6), repeated here for convenience,

$$d(\sin\theta_r - \sin\theta_i) = m\lambda \tag{6}$$

for θ_r as a function of θ_i and adding a ridge to the model along a line for each diffraction order. However, for out-of-plane data, these diffraction orders require coordinate transforms into spherical coordinates, and become functions of the orientation of the grating. While it is possible to produce these equations, scatter from diffraction gratings is a well-understood phenomenon, and this modeling effort is aimed at features unique to PC structures.

Modeling data out of the plane of incidence

While there was hope that the relatively simple ridges of the in-plane model would be applicable to an out-of-plane model, this does not seem to be the case for the ridges at a constant θ_r, which would have produced a cone around the surface normal, similar to Figure 23. There does appear to be conical ridge structures present in the 3-D data, but they appear to be functions of θ_i and θ_r, simultaneously, and more 3-D data would be required to characterize these.

The ridge at a constant θ_i appears to be accurate, and is seen in Figure 19 as the overall larger hemisphere for $\theta_i = 25°$ for *s*-polarization, and can be seen in Figure 24 compared to the actual data at $\theta_i = 25°$ and the data and model at 15° and 35°. Beyond this feature, the out-of-plane data shows significantly more complexity than this modeling effort can address in the time allowed.

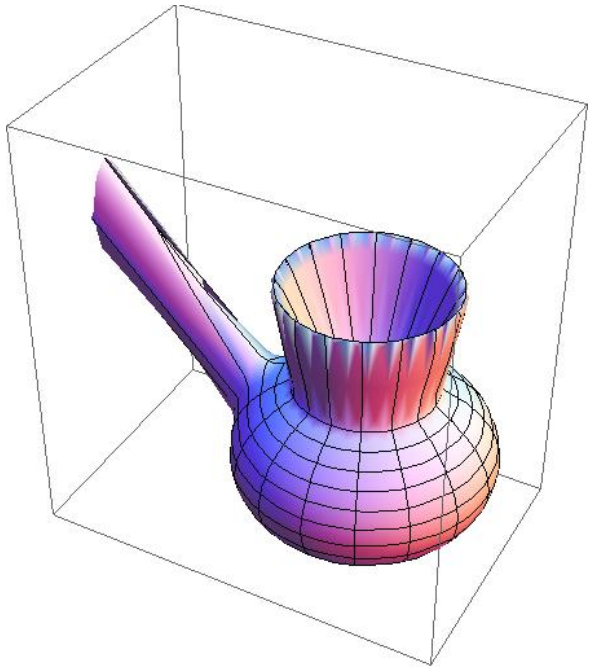

Figure 23. Sandford-Robinson model with a ridge at $\theta_r = 17°$.

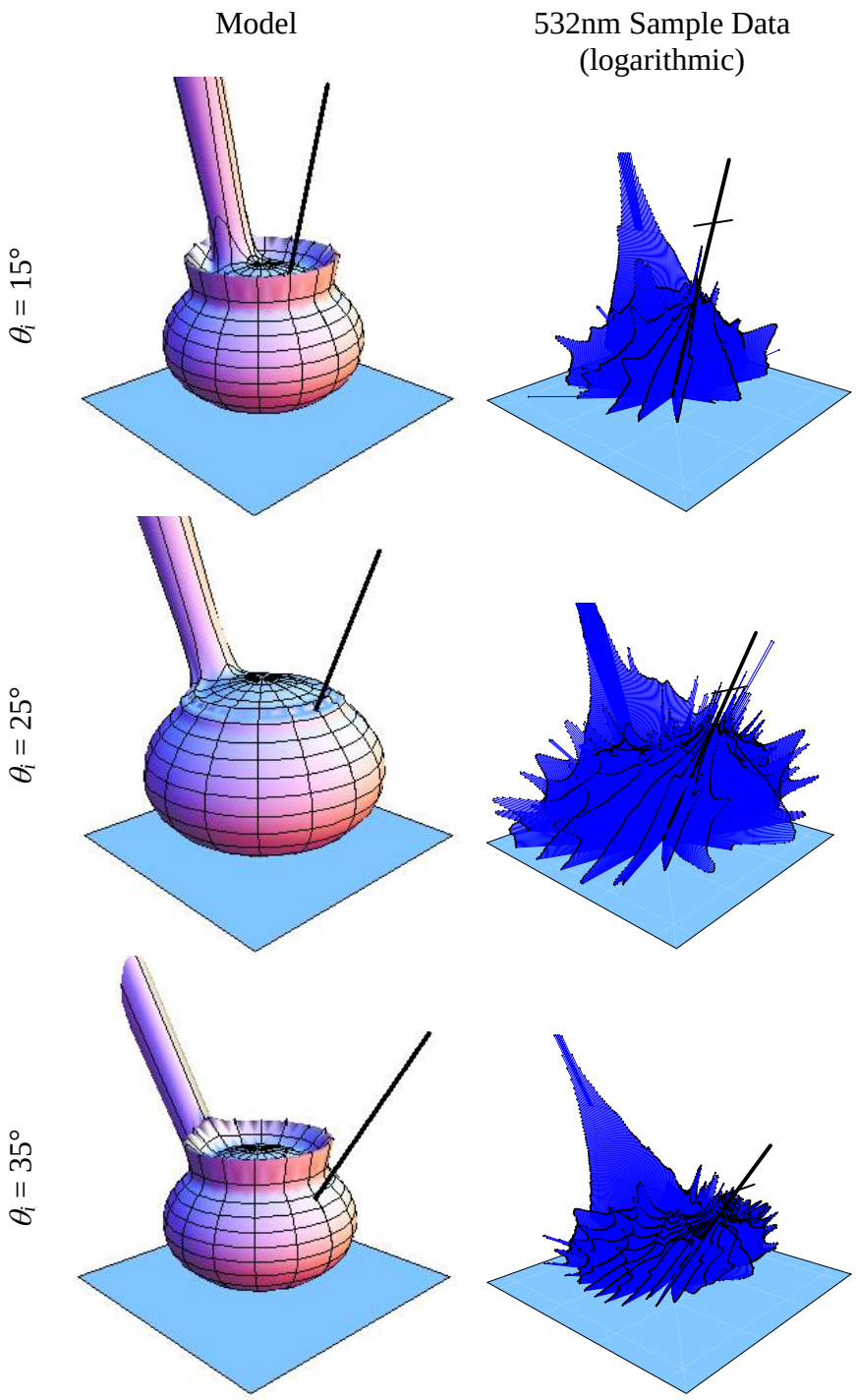

Figure 24. Comparison of the modified Sandford-Robinson model and the BRDF data collected from the 532nm sample, measured at 544nm, *s*-polarization, for three different incident angles. The scale for the three models is the same, as is the logarithmic scale for the three sets of actual data.

Summary

While the alterations of Equations (22)-(24) applied to the Sandford-Robinson model might be suitable to produce accurate results when compared to in-plane data, they do not appear to be suitable to model the complex peaks seen at the resonant angle the out-of-plane data. Until more out-of-plane data is collected with smaller apertures and smaller steps in θ_i, further development of this model has been suspended. However, the current form may still be useful for some applications.

The only feature successfully modeled on the out-of-plane data was the increase in reflectance in all directions for the "resonant" θ_i. To fully understand the other features of the out-of-plane reflectance, finer steps in the rotation of the slices are needed, as well as the use of smaller apertures on the CASI. With the current method of collecting out-of-plane measurements, this would be an extremely time consuming procedure, and prone to human error in setting the correct rotations.

VI. Conclusions and Recommendations

In this research, the goal was to analyze the scatter off of photonic crystal structures and create a model of this scatter suitable for incorporation into scene rendering software. The first step was to analyze the spectral transmittance of the structures as a function of the incident angle. Then, the scatter in the plane of incidence was analyzed, which identified a resonant angle which was dependent on the difference between the laser wavelength and the wavelength of minimum transmission. The scatter out-of-plane was then analyzed using the resonant angle and two nearby angles as the incident angles. The results from the in-plane and out-of-plane data were then modeled using the Sandford-Robinson model, modified to attempt to account for the unusual features seen in the scatter pattern.

Conclusions of Research

The type of PC structure analyzed was designed for specific wavelengths and was analyzed using lasers slightly off from these wavelengths. There is a resonant angle that depends on this wavelength difference. For incident light at this resonant angle, the total hemispherical reflectance increases, effectively causing the structure to "glow." There is also significant structure in the pattern of this increase reflectance, but equipment and time limitations precluded a full investigation. For light leaving the structure at the resonant angle, the reflectance is always significantly stronger than the average reflectance over the hemisphere, and does not change significantly due to incident angle.

Significant Contribution of this Research

While laboratory equipment similar to the CASI system has been in use for some time, to the best of my knowledge after searching the literature, this research is the first time that the in-plane or out-of-plane scatter from a photonic crystal structure has been quantitatively measured. It also laid the groundwork for future investigation of the reflectance properties of other anisotropic materials, and suggests that any BRDF modeling of these structures will need to be functions of $\Delta\lambda$, ψ_i, and ψ_r, in addition to the normal θ_i, ϕ_i, θ_r, ϕ_r variables .

Recommendations for Action: Tunable lasers

Two of the samples suggested a relationship between a sample's resonant angle and $\Delta\lambda$, the difference between the laser wavelength and the minimum transmittance. While other research into the scatter of PC structures also suggests this type of relationship [5], other measurements must be taken at other wavelengths to confirm this. In order to understand the relationship, small steps in wavelength are required, which requires a tunable laser. While coupling additional lasers into the beam path in a source box should not be difficult, any changes in wavelength will likely have to be done by hand, similar to switching between lasers in the current CASI setup.

Recommendations for Action: Automated out-of-plane collection

For out-of-plane data collection, there are several relatively simple additions to the CASI setup which would make data collection faster and less prone to human error. While adding CASI control to ψ_i, ψ_r, β, and γ would require modification of the software and hardware, simply adding stand-alone motor control to ψ_i, β, and γ should not be

nearly as complex. This would still require human input of the correct values, but it would be more precise than using the existing scales, and there would be no human error due to misreading the scales.

As stated earlier, the ψ_r value for out-of-plane data is dependent on the receiver position, δ, and so it is not possible to analyze the polarization of the reflected light without incorporating control of ψ_r into the CASI software. However, if the software and hardware were able to be modified to include ψ_i, ψ_r, β, and γ control, it would significantly reduce the time required to obtain 3-D BRDF data, and require minimal human intervention. However, it would require ensuring that the illuminated area of the sample does not move as β and γ are changed, which may prove to be difficult with the current sample holders.

Additionally, whenever ψ_i is changed, it will be necessary to recollect the Total Signal measurement, which will ensure that the BRDF for that collection is scaled properly. This would require motorization of the stage translation axes to move the sample and the sample mount out of the beam path. The best way of accomplishing this would be to have a "safe position" where it is known that the beam path is unobstructed, and having the CASI move the stages to this position, collect the Total Signal, and return the sample to the original location. While ideally the Total Signal measurement should not change when ψ_i is rotated using a half-wave plate, the half-wave plate will create an elliptical polarization if tunable lasers are used and the laser wavelength moves away from the wave plate's design wavelength. This then requires the use of a polarizer to ensure the incident polarization is as linear as possible, but will decrease the power of the beam.

One final concern with automated out-of-plane measurements is the sample mount. As β and γ were rotated for this experiment, parts of the mount blocked the receiver near grazing angles. Aside from producing incorrect data, this significantly increases collection time, as the CASI attempts to integrate the non-existent signal for longer periods of time. This problem is less important with rigid samples which can be mounted near the front edge of the holder, but remains significant for flexible samples, such as the 532nm, sample which must be held flat by the mount.

Recommendations for Action: PC BRDF Development

Initial efforts at modeling the BRDF from the PC samples did not accurately model the complex peaks seen out of the plane of incidence, and were only able to model the in-plane results as a first approximation. To improve the model, more out-of-plane data needs to be collected with smaller apertures, finer steps in the rotation of the slices, and smaller steps in θ_i. All of these tasks will be significantly faster and easier with an automated collection system.

Summary

While the obstacles to incorporating tunable lasers and automating out-of-plane measurements may be significant, they are likely considerably less expensive than custom built systems similar to those used by the Air Force Research Laboratory for similar data collection. Allowing the rapid collection of out-of-plane reflectance data at multiple wavelengths will allow AFIT to take a leading role in investigating new photonic crystal materials, and confirming the theoretical models which are used to produce them.

This research looked at the optical properties of three photonic crystal structures, concentrating on their reflectance out of the plane of incidence. While these materials themselves may not prove to be significant, a procedure has been established which will allow similar analysis of other structures. As PC materials continue to become cheaper, larger, and more widespread, this type of analysis will prove vital as part of unlocking potential applications of these novel structures.

Appendix A. 532nm Sample Data

Collinear Spectral Transmittance

Mesh lines along the incident axis are the actual data points.
Mesh lines along the wavelength axis are 532nm (λ_{Tmin}) and 544nm (λ_{laser}).

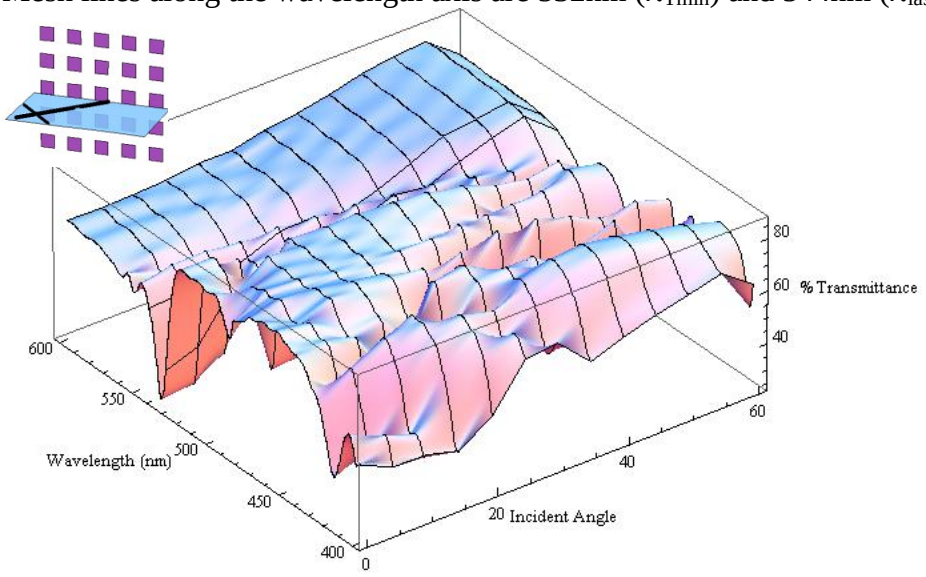

Figure 25. Collinear spectral transmittance of the 532nm sample as a function of incident angle for *p*-polarized incident light, as shown in the subfigure.

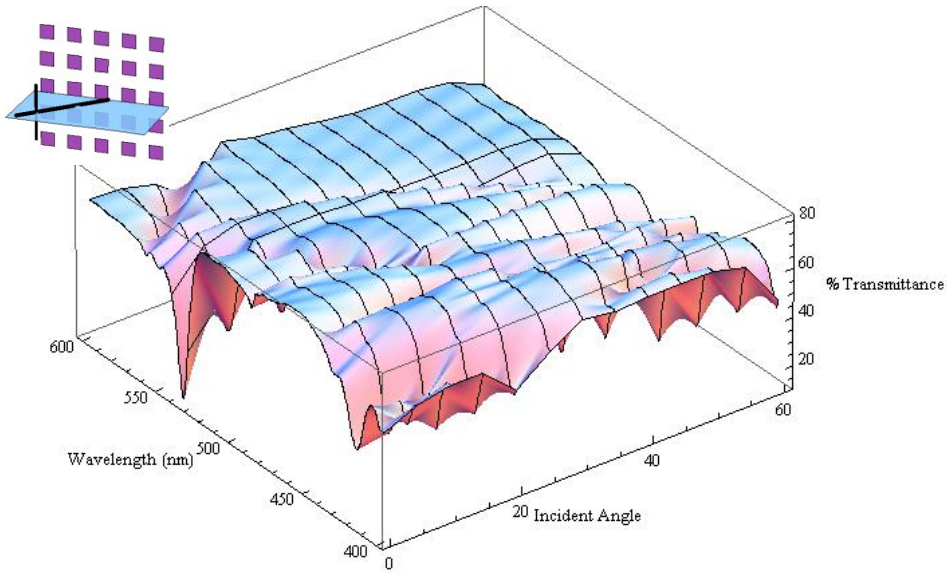

Figure 26. Collinear spectral transmittance of the 532nm sample as a function of incident angle for *s*-polarized incident light, as shown in the subfigure.

In-plane BRDF Data: 532nm sample measured at 544nm

$\Delta\lambda$ = 11.5nm when illuminated by the 544 laser

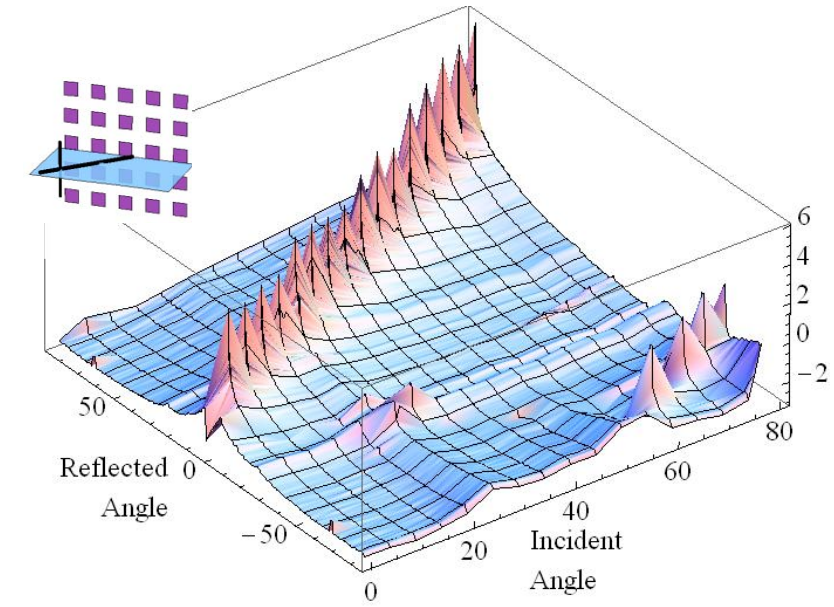

Figure 27. Plot of Log_{10}(BRDF) for 532nm sample, *s*-polarization. The subfigure shows the polarization relative to the incident plane and the PC structure.

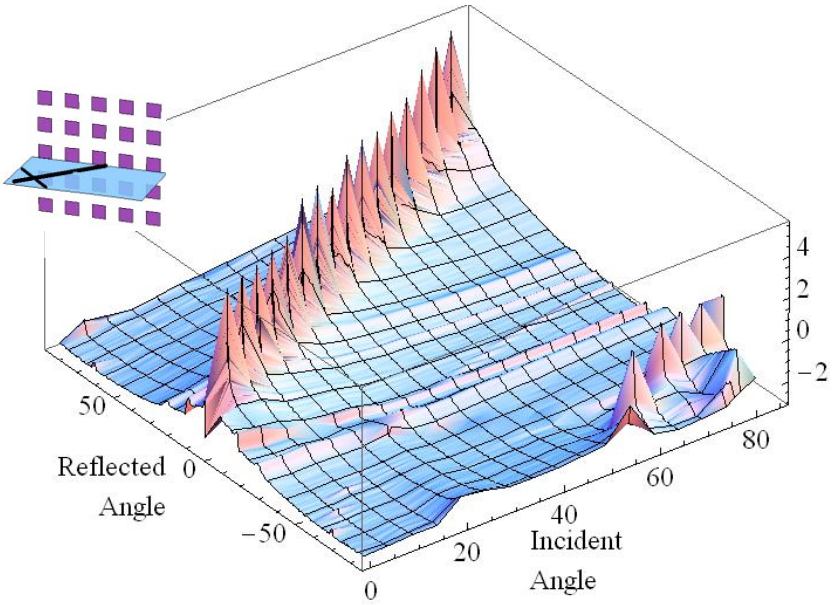

Figure 28. Plot of Log_{10}(BRDF) for 532nm sample, *p*-polarization. The subfigure shows the polarization relative to the incident plane and the PC structure.

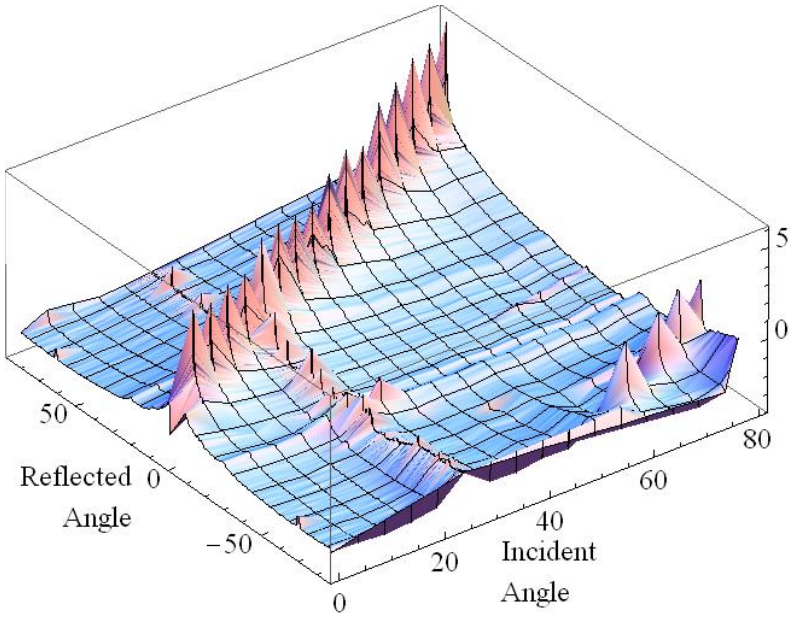

Figure 29. Replotting of Figure 27 (532nm sample, *s*-polarization), using smaller appertures for θ_i = 25° to analyze the peak seen there.

In-plane BTDF Data: 532nm sample measured at 544nm

$\Delta\lambda$ = 11.5nm when illuminated by the 544 laser

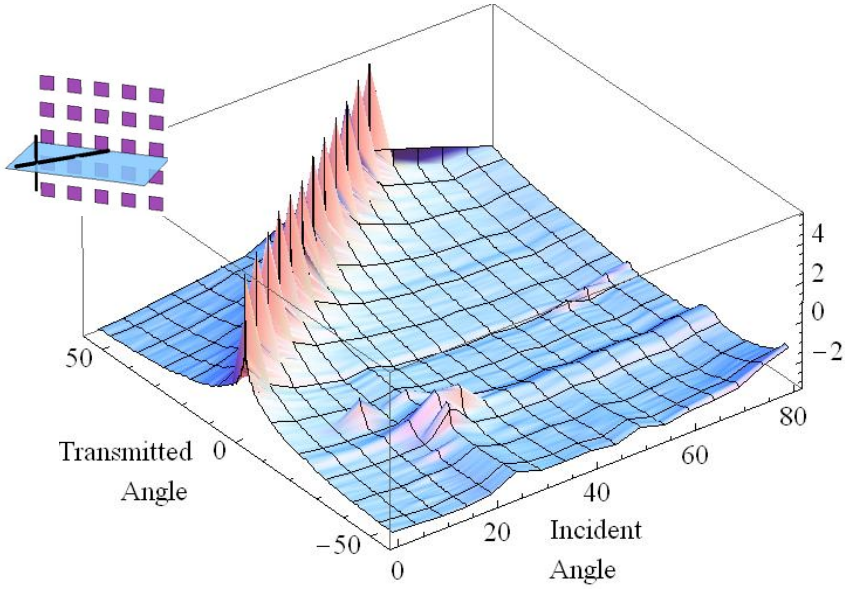

Figure 30. Plot of Log_{10}(BTDF) for 532nm sample, *s*-polarization. The subfigure shows the polarization relative to the incident plane and the PC structure.

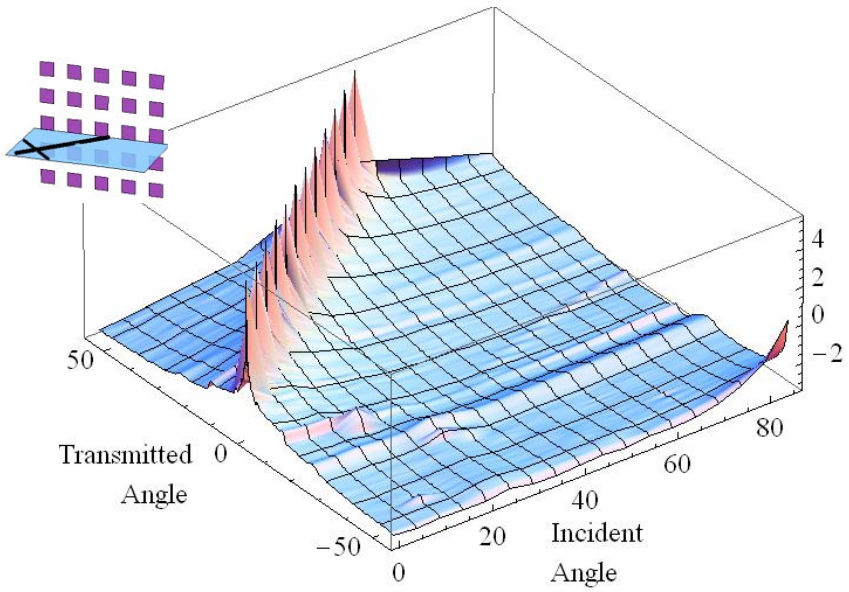

Figure 31. Plot of Log_{10}(BTDF) for 532nm sample, *p*-polarization. The subfigure shows the polarization relative to the incident plane and the PC structure.

Appendix B. 633nm Sample Data

Collinear Spectral Transmittance

Mesh lines along the incident axis are the actual data points.
Mesh line along wavelength axis is 644nm (laser and stated sample wavelength).

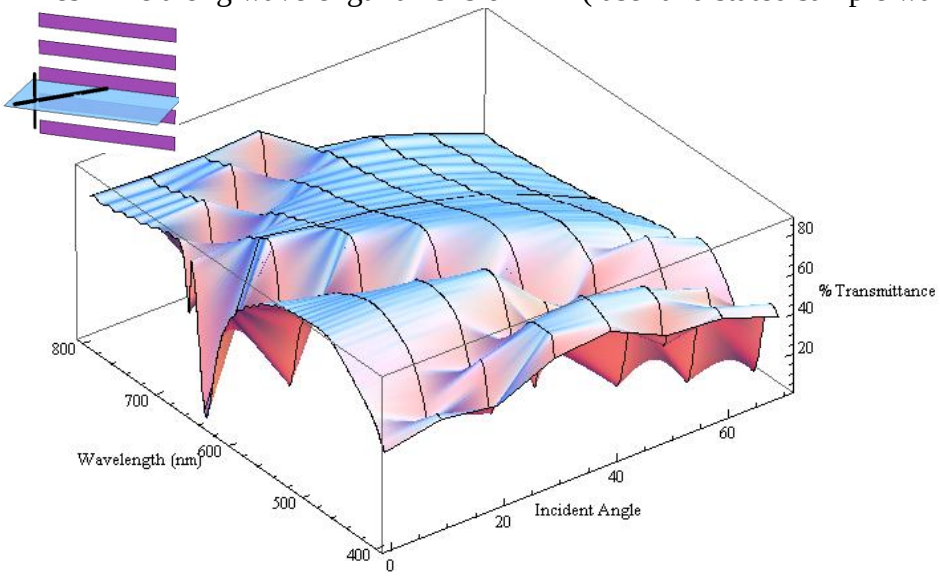

Figure 32. Collinear spectral transmittance of the 644nm sample as a function of incident angle for *s*-polarized incident light, with grating parallel to the plane of incidence, as shown in the subfigure.

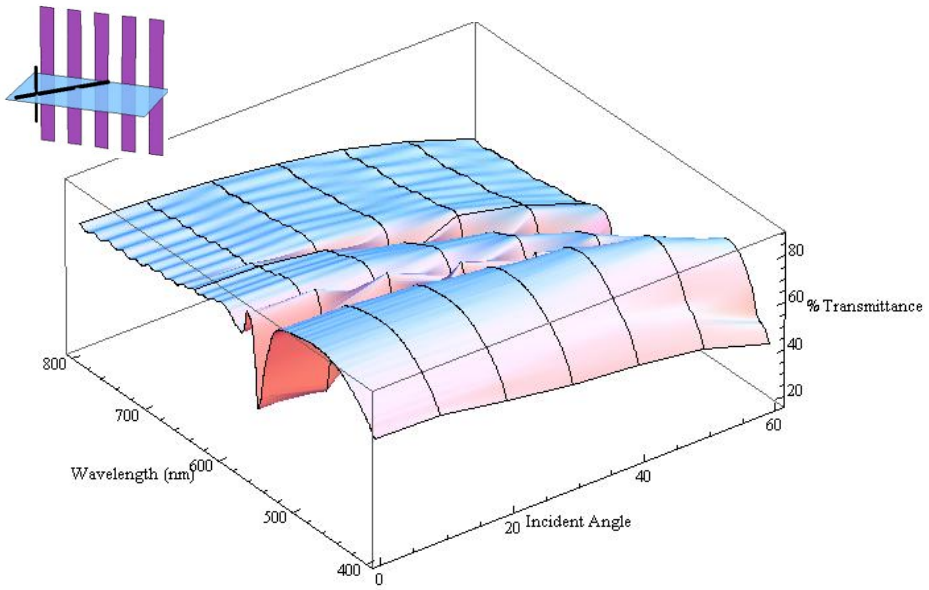

Figure 33. Collinear spectral transmittance of the 644nm sample as a function of incident angle for *s*-polarized incident light, with grating perpendicular to the plane of incidence, as shown in the subfigure.

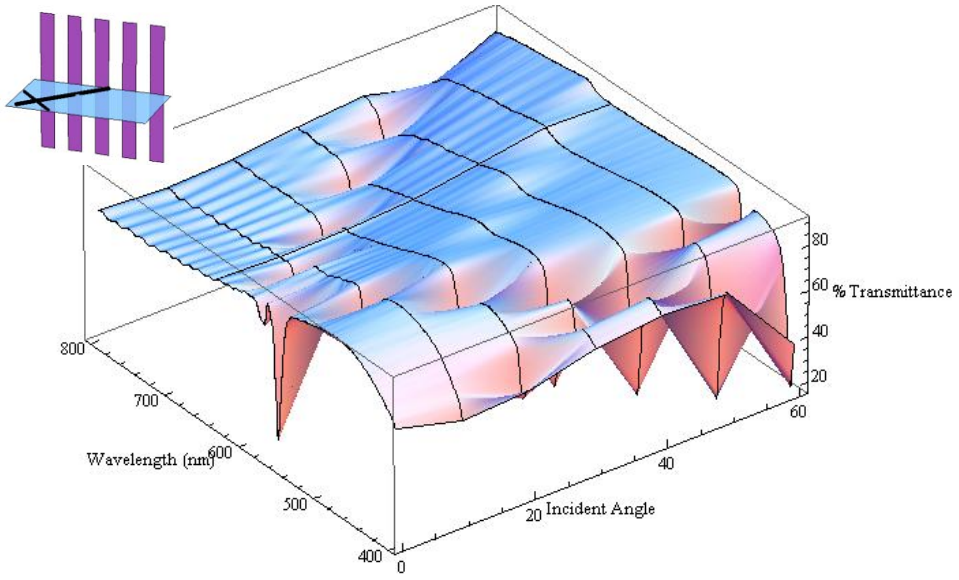

Figure 34. Collinear spectral transmittance of the 644nm sample as a function of incident angle for *p*-polarized incident light, with grating perpendicular to the plane of incidence, as shown in the subfigure.

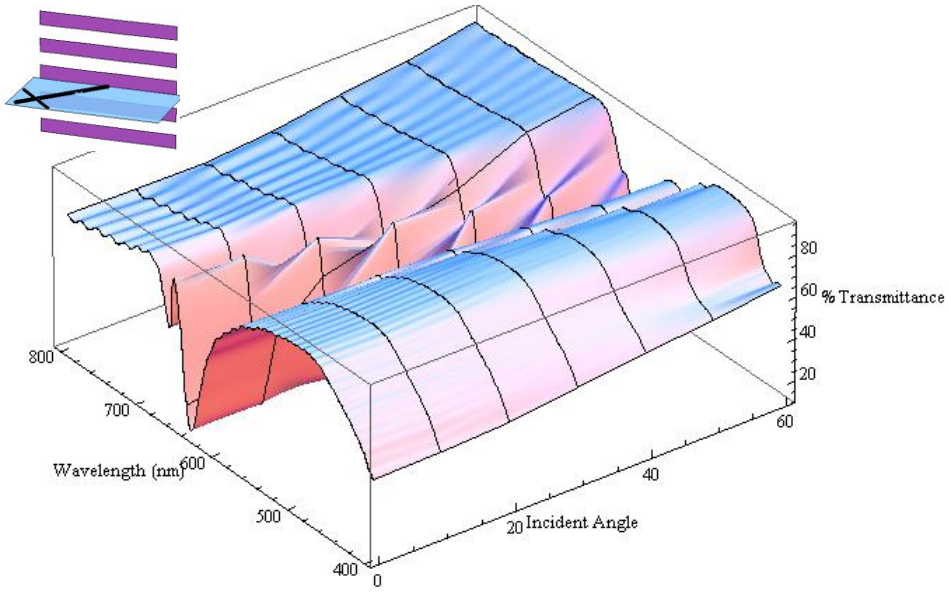

Figure 35. Collinear spectral transmittance of the 644nm sample as a function of incident angle for *p*-polarized incident light, with grating parallel to the plane of incidence, as shown in the subfigure.

In-plane BRDF Data: 633nm sample measured at 633nm

$\Delta\lambda$ = 5nm, 74nm when illuminated by the 633nm laser

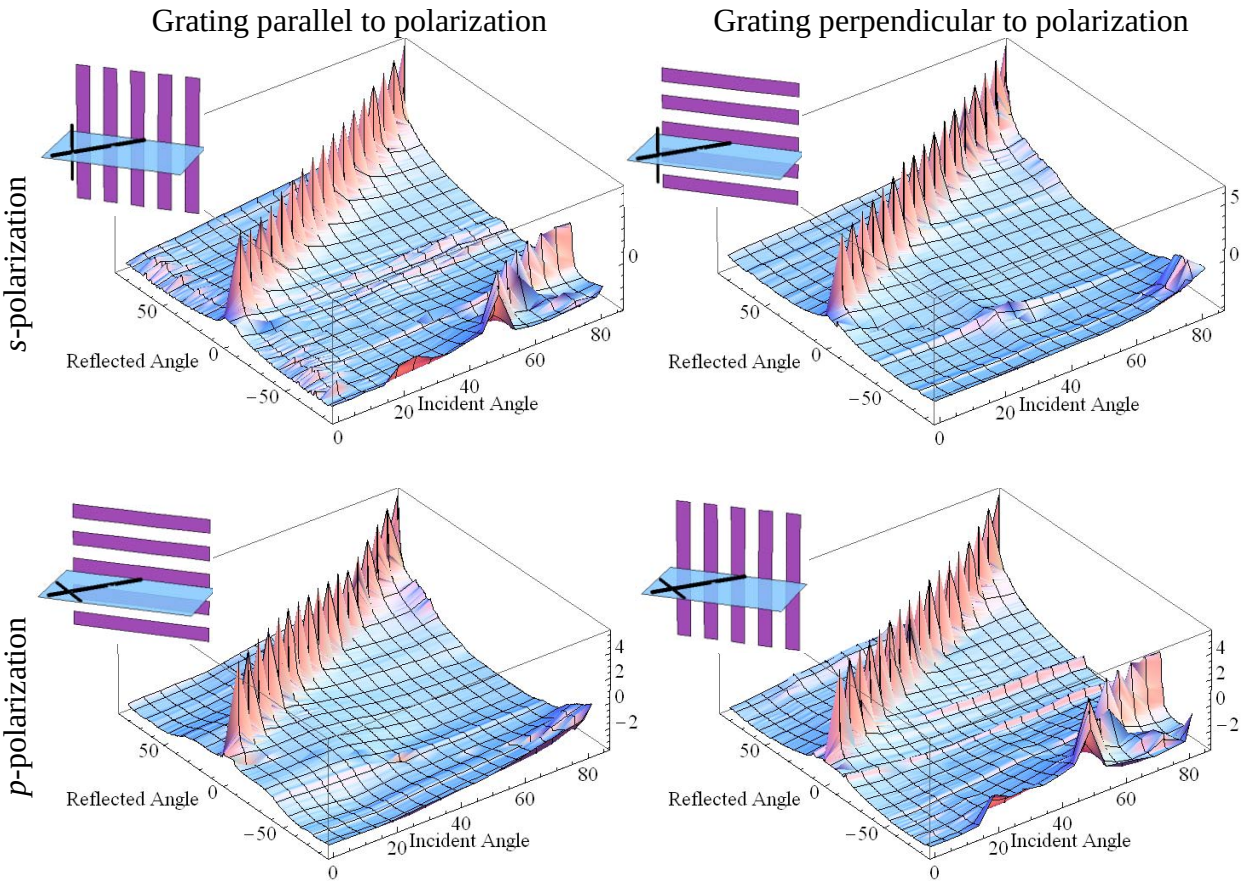

Figure 36. Log_{10}[BRDF] of the 633nm sample measured by a 633nm laser, for *s*- and *p*-polarization, and for the grating perpendicular and parallel to the incident polarization. The subfigures show the grating and polarization relative to the incident plane.

In-plane BRDF Data: 633nm sample measured at 544nm

$\Delta\lambda$ = 15nm and 94nm when illuminated by the 544 laser

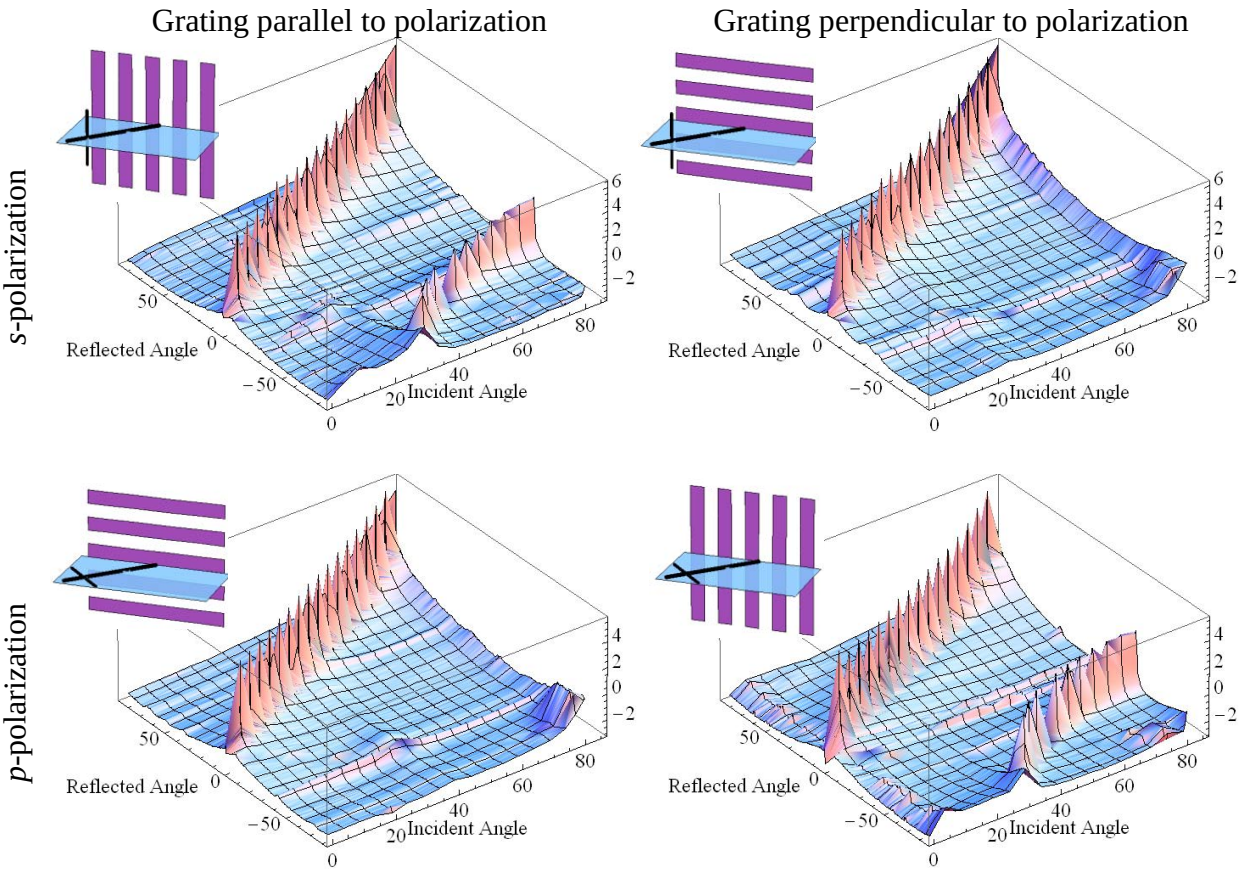

Figure 37. Log_{10}[BRDF] of the 633nm sample measured by a 544nm laser, for *s*- and *p*-polarization, and for the grating perpendicular and parallel to the incident polarization. The subfigures show the grating and polarization relative to the incident plane.

In-plane BTDF Data: 633nm sample measured at 633nm

$\Delta\lambda$ = 5nm and 74nm when illuminated by the 633nm laser

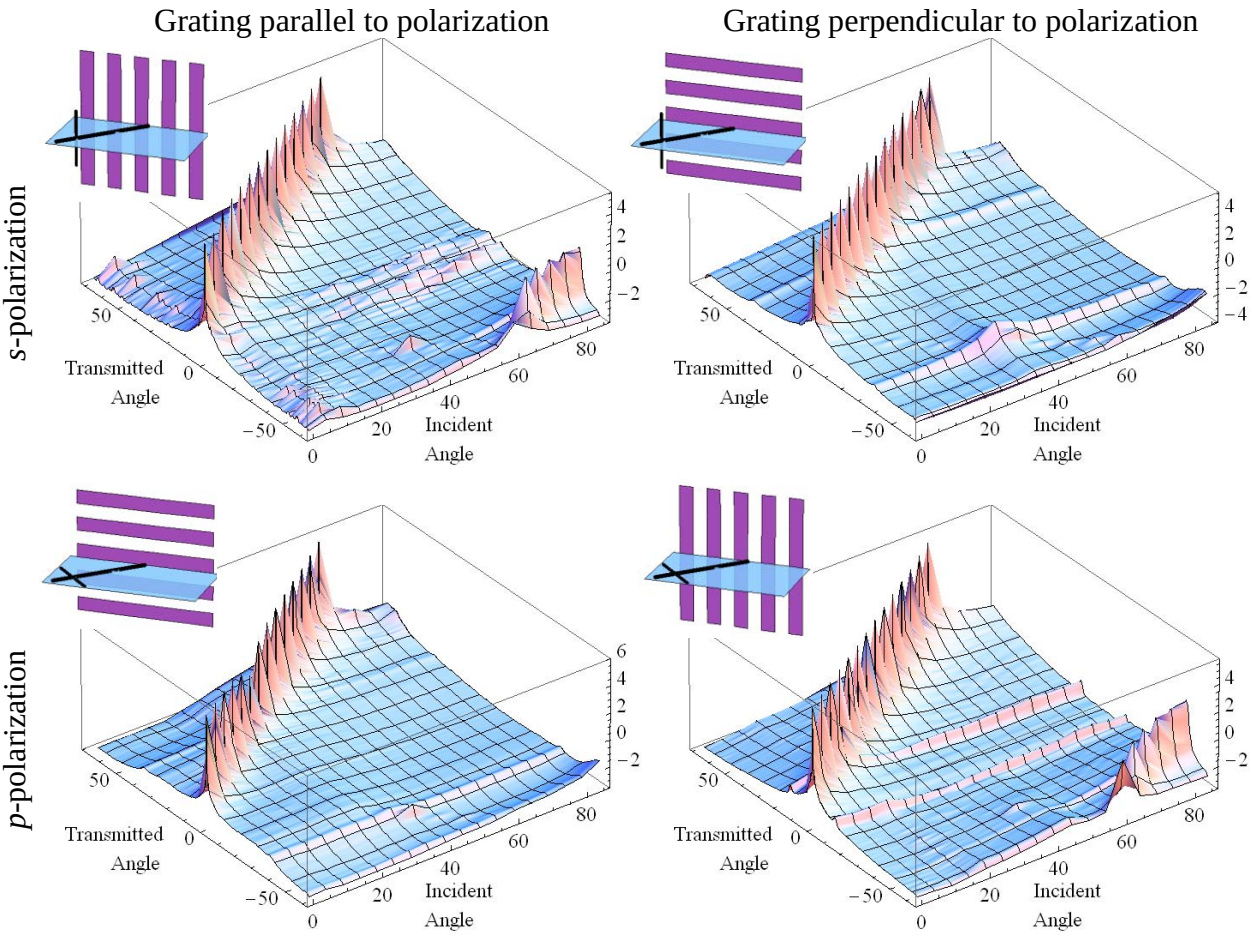

Figure 38. Log_{10}[BTDF] of the 633nm sample measured by a 633nm laser, for *s*- and *p*-polarization, and for the grating perpendicular and parallel to the incident polarization. The subfigures show the orientation of the grating and polarization relative to the incident plane.

In-plane BTDF Data: 633nm sample measured at 544nm

$\Delta\lambda$ = 15nm and 94nm when illuminated by the 544 laser

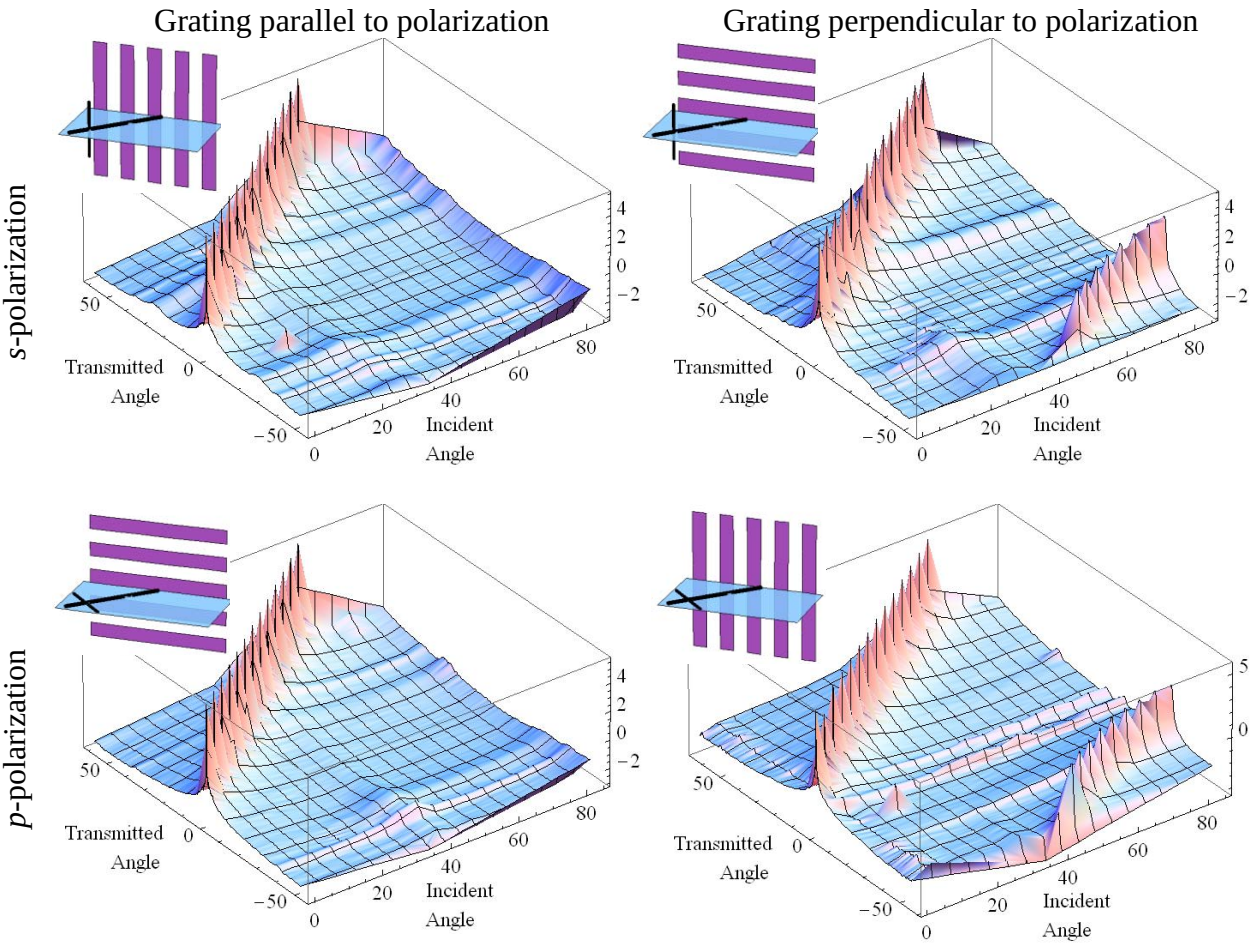

Figure 39. Log_{10}[BTDF] of the 633nm sample measured by a 544nm laser, for *s*- and *p*-polarization, and for the grating perpendicular and parallel to the incident polarization. The subfigures show the grating and polarization relative to the incident plane.

Appendix C. 3.39μm Sample Data

Collinear Spectral Transmittance

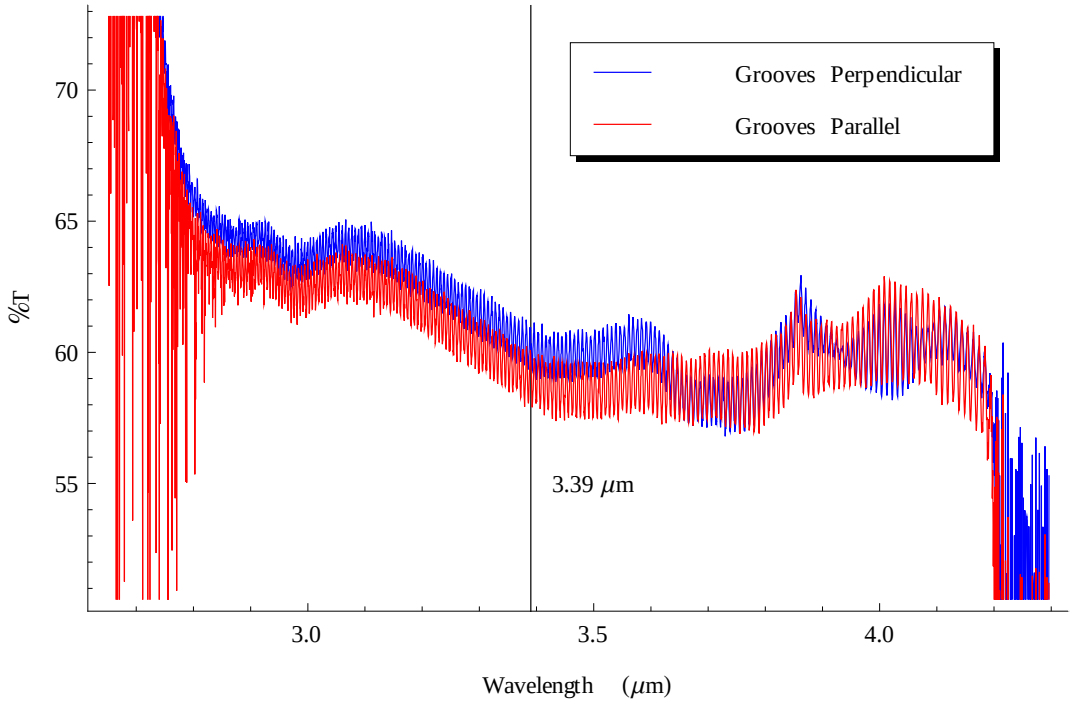

Figure 40. Collinear spectral transmittance spectrum for 3.39μm sample at normal incidence, with the grooves parallel and perpendicular to the incident polarization

In-plane BRDF Data: 3.39μm sample measured at 3.39μm

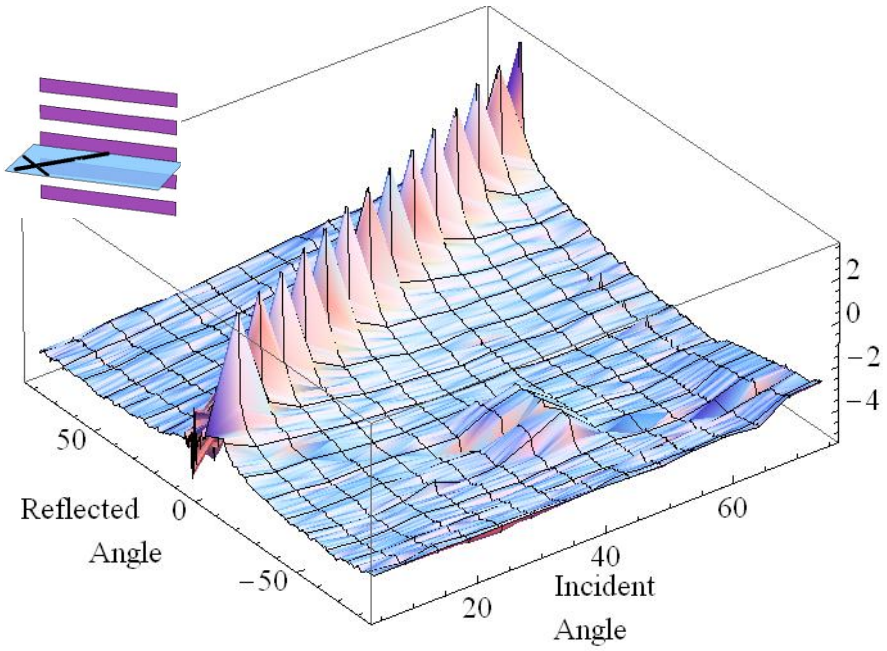

Figure 41. Log_{10}[BRDF] of the 3.39µm sample measured by a 3.39μm laser, for *p*-polarization and the grating perpendicular to the incident polarization. The subfigure shows the orientation of the grating and polarization relative to the incident plane.

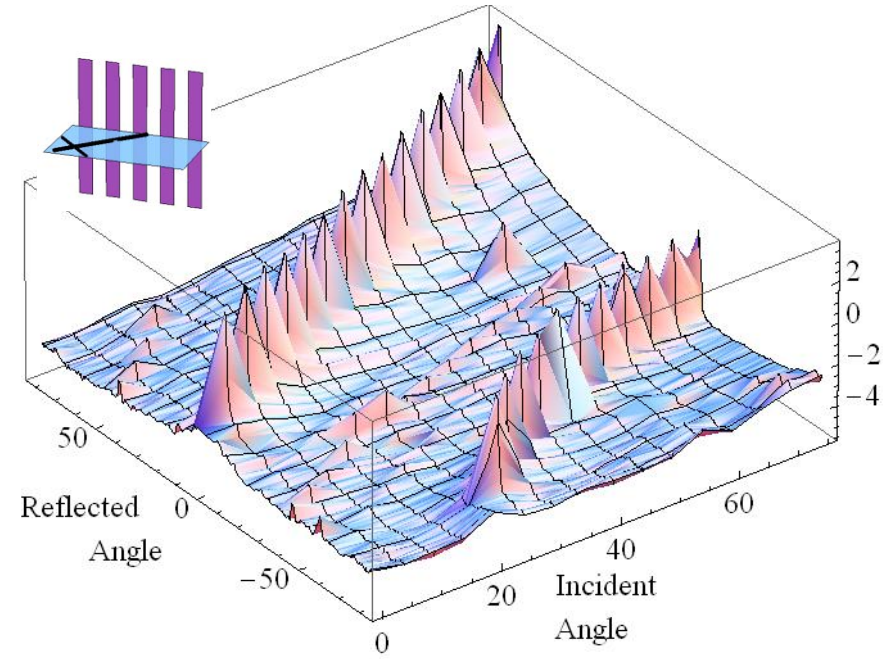

Figure 42. Log_{10}[BRDF] of the 3.39μm sample measured by a 3.39μm laser, for *p*-polarization and the grating parallel to the incident polarization. The subfigure shows the orientation of the grating and polarization relative to the incident plane.

In-plane BTDF Data: 3.39μm sample measured at 3.39μm

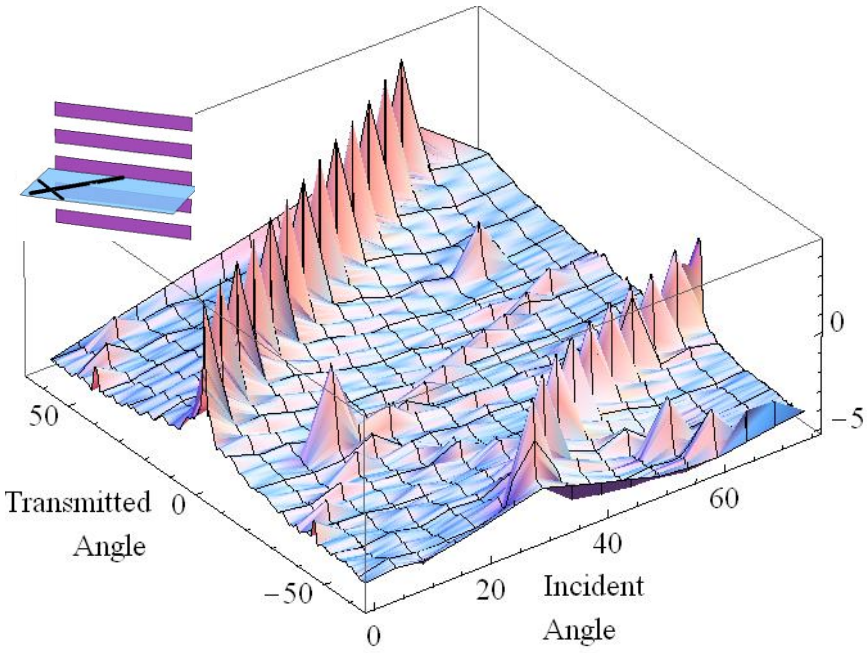

Figure 43. Log_{10}[BTDF] of the 3.39μm sample measured by a 3.39μm laser, for *p*-polarization and the grating perpendicular to the incident polarization. The subfigure shows the orientation of the grating and polarization relative to the incident plane.

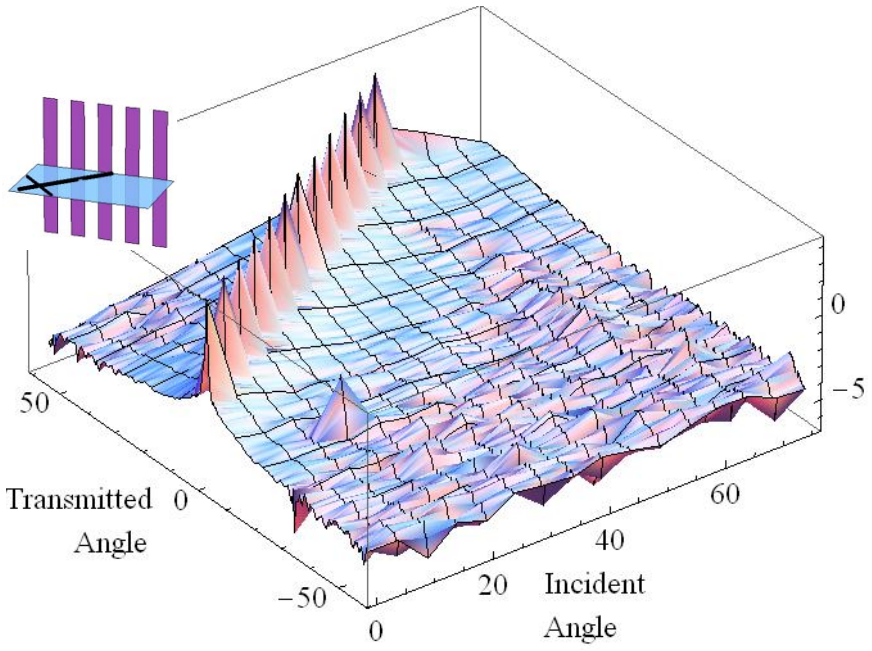

Figure 44. Log_{10}[BTDF] of the 3.39μm sample measured by a 3.39μm laser, for *p*-polarization and the grating parallel to the incident polarization. The subfigure shows the orientation of the grating and polarization relative to the incident plane.

Appendix D. Mathematica Code

Exporting and plotting in-plane CASI data

```
(* Data must be in files named "MyData XX.CSV", where XX is the incident angle.
  "MyData" should be a descriptive name of the collection set*)
dir = "D:\\Data Directory Path\\MyData ";
offset = 17; (* First good data point in all files, including header lines *)
end = 7; (*number of bad data points at end of file, due to sample mount obstruction*)
ObstructionError = 0; (* angle error for reflections at θi=85,
due to incorrect angles with ocultation, must be fitted individually. *)

data00 = Import[StringJoin[dir, "00.csv"], "CSV"];
data05 = Import[StringJoin[dir, "05.csv"], "CSV"];
data10 = Import[StringJoin[dir, "10.csv"], "CSV"];
(* Repeat for all angles *)
data80 = Import[StringJoin[dir, "80.csv"], "CSV"];
data85 = Import[StringJoin[dir, "85.csv"], "CSV"];

(* Corrects reflected angle and creates 3D points *)
data00correct = Table[{x = 0, data00[[i, 1]], data00[[i, 2]]}, {i, offset, Length[data00] - end}];
data05correct = Table[{x = 5, x + data05[[i, 1]], data05[[i, 2]]}, {i, offset, Length[data05] - end}];
data10correct = Table[{x = 10, x + data10[[i, 1]], data10[[i, 2]]}, {i, offset, Length[data10] - end}];
(* Repeat for all angles*)
data80correct = Table[{x = 80, x + data80[[i, 1]], data80[[i, 2]]}, {i, offset, Length[data80] - end}];
data85correct = Table[{x = 85, ObstructionError + x + data85[[i, 1]], data85[[i, 2]]},
   {i, offset, Length[data85] - end}];

AllData = Join[data00correct, data05correct, data10correct, data15correct, data20correct,
   data25correct, data30correct, data35correct, data40correct, data45correct, data50correct,
   data55correct, data60correct, data65correct, data70correct, data75correct, data80correct,
   data85correct];

(* Exports combined file into source directory, format is (θi, θr, BRDF) *)
Export[StringJoin[dir, "data.csv"], AllData];

(* Converts BRDF to Log[BRDF] and plots data*)
AllLogData = Table[{AllData[[i, 1]], AllData[[i, 2]], Log[Abs[AllData[[i, 3]]]]},
   {i, Length[AllData]}];
ListPlot3D[AllLogData, AxesLabel → {"Incident Angle", "Reflected Angle"}, PlotRange → Full,
 ViewPoint → {-30, -40, 30}, ViewAngle → All,
 Mesh → {Table[x, {x, 0, 85, 5}], Table[x, {x, -80, 80, 10}]}]
```

Generating list of angles for out-of-plane CASI measurements

Note: The code for solving for γ comes from Equation (9):

$$\phi_i = \arctan\begin{pmatrix} -\cos\gamma\sin\alpha - \cos\alpha\sin\beta\sin\gamma, \\ \cos\alpha\cos\gamma\sin\beta - \sin\alpha\sin\gamma \end{pmatrix} \tag{9}$$

By setting $\phi_i = 0°$, the first argument of the arctangent must be 0, resulting in

$$\cos\gamma\sin\alpha = -\cos\alpha\sin\beta\sin\gamma \tag{25}$$

However, the direction of all rotations except γ are reversed in the AFIT laboratory, relative to the system which these equations were based on. By mirroring the entire system and then reversing γ, the rotations match the AFIT system, and Equation (25) becomes

$$\begin{gathered} \cos(-\gamma)\sin\alpha = -\cos\alpha\sin\beta\sin(-\gamma) \\ \cos(\gamma)\sin\alpha = \cos\alpha\sin\beta\sin(\gamma) \end{gathered} \tag{26}$$

which correctly solves for γ as a positive value, based on the rotations in Figure 17.

```
β[θi_, α_] := β /. FindRoot[θi == ArcCos[Cos[α] Cos[β]], {β, 45 °}]
ψ[α_, β_] := ArcTan[-Sin[β], Cos[β] Sin[α]]
γ[α_, β_] := γ /. FindRoot[Cos[γ] Sin[α] == Cos[α] Sin[β] Sin[γ], {γ, 45 °}]
Do[
 Print[Row[{"For θi = ", θi 180/π, "° :  "}]]
  Do[
   Print[Row[{"α = ", α 180/π,
      "° ;  β = ", β[θi, α] 180/π,
      "° ;  γ = ", γ[α, β[θi, α]] 180/π,
      "° ;  ψi = ", 180 - ψ[α, β[θi, α]] 180/π, "°"}]], {α, 0, θi - 1 °, 5 °}]
  Print[Row[{"α = ", θi, " ;  β = 0° ;  γ = ", γ[θi, 0] 180/π, "° ;  ψi = ", 180 - ψ[θi, 0] 180/π, "°"}]]
, {θi, 5 °, 60 °, 5 °}]
```

Plotting out-of-plane CASI data

```
(* Data must be in files named "MyData XX.CSV", where XX is the α angle, equivalent to θi from in plane data.
  "MyData" should be a descriptive name of the collection set*)
dir = StringJoin["D:\\Data Directory Path\\MyData "];
offset = 13; (* First good data point in all files, including header lines *)
end = 1; (*number of bad data points at end of file, due to sample mount obstruction*)

data00 = Import[StringJoin[dir, "00.csv"], "CSV"];
data05 = Import[StringJoin[dir, "05.csv"], "CSV"];
data10 = Import[StringJoin[dir, "10.csv"], "CSV"];
data15 = Import[StringJoin[dir, "15.csv"], "CSV"];


(*Normally results in (θi,θr,BRDF).  For 3D case, results are Germer's notation (α,δ,BRDF)  *)
(*added γ as 4th element, β as 5th*)
data00correct = Table[{x = 0, data00[[i, 1]], data00[[i, 2]], 0, 15}, {i, offset, Length[data00] - end}];
data05correct = Table[{x = 5, x + data05[[i, 1]], data05[[i, 2]], 19.6786, 14.1602}, {i, offset, Length[data05] - end}];
data10correct = Table[{x = 10, x + data10[[i, 1]], data10[[i, 2]], 42.1385, 11.2378}, {i, offset, Length[data10] - end}];
data15correct = Table[{x = 15, x + data15[[i, 1]], data15[[i, 2]], 90, 0}, {i, offset, Length[data15] - end}];

AllData = Join[data00correct, data05correct, data10correct, data15correct];
Export[StringJoin[dir, "3D data Germer Notation.csv"], AllData]

LogOffset = 10; (* makes all Log values positive*)

(** α=5°, repeat for all α values, changing the source data and the final data*********************)
datacorrect = data05correct;  (* change for each source data*)
γ = -datacorrect[[1, 4]];
β = -datacorrect[[1, 5]];
Data = Table[{
    (Log[datacorrect[[i, 3]] + LogOffset) Sin[datacorrect[[i, 2]] °],
    0,
    (Log[datacorrect[[i, 3]] + LogOffset) Cos[datacorrect[[i, 2]] °]}, {i, Length[datacorrect]}];
Dataβ = Table[{
    Data[[i, 1]],
    Data[[i, 2]] Cos[β] - Data[[i, 3]] Sin[β],
    Data[[i, 2]] Sin[β] + Data[[i, 3]] Cos[β]
   }, {i, Length[Data]}];
(* change for each source data*)
Data05 = Table[{
    Dataβ[[i, 1]] Cos[γ] - Dataβ[[i, 2]] Sin[γ],
    Dataβ[[i, 1]] Sin[γ] + Dataβ[[i, 2]] Cos[γ],
    Dataβ[[i, 3]]}, {i, Length[Dataβ]}];
(* change for each source data*)
Data05m = Table[{
    -Dataβ[[i, 1]] Cos[γ] - Dataβ[[i, 2]] Sin[γ],
    Dataβ[[i, 1]] Sin[γ] + Dataβ[[i, 2]] Cos[γ],
    Dataβ[[i, 3]]}, {i, Length[Dataβ]}];
(** End repeated section ***********************************************************)
```

```
OffAxisData = Join[Data05, Data10, Data05m, Data10m];
BRDF =
  Graphics3D[GraphicsComplex[OffAxisData, Table[{PointSize[.005], Black, Point[i], Blue, Line[{1, i}]},
     {i, 2, Length[OffAxisData]}]], PlotRange → {{-7, 7}, {-7, 7}, {-5, 9}}, ViewPoint -> {1, .9, .5},
   ViewVertical → {0, 0, 1}, ViewAngle → 40 °, Boxed → False];
θi = 15 °;
(*lines to denote direction and polarization of incident light, and a plane to represent the surface*)
Incident = Graphics3D[{Polygon[{{5, 5, 0}, {5, -5, 0}, {-5, -5, 0}, {-5, 5, 0}}], Thickness[.01],
    Line[{{0, 9 Sin[θi], 9 Cos[θi]}, {0, 0, 0}}]}];
ppol =
  Graphics3D[
   {Thickness[.005],
    Line[{{0, 7 Sin[θi] + Cos[θi], 7 Cos[θi] - Sin[θi]}, {0, 7 Sin[θi] - Cos[θi], 7 Cos[θi] + Sin[θi]}}]}];
spol = Graphics3D[{Thickness[.005],
    Line[{{1, 7 Sin[θi], 7 Cos[θi]}, {-1, 7 Sin[θi], 7 Cos[θi]}}]}];
Show[{BRDF, Incident, ppol}]
```

Bibliography

[1] (2005, January) USAToday. [Online]. http://www.usatoday.com/travel/news/2005-01-04-laser-aircraft_x.htm

[2] J. D. Joannopoulos, S. G. Johnson, J. N. Winn, and R. D. Meade, *Photonic Crystals: Molding the Flow of Light*, Second Edition ed. Princeton, New Jersey: Princeton University Press, 2008.

[3] J.-M. Lourtioz, "Photonic crystals and metamaterials," *C. R. Physique*, vol. 9, pp. 4-15, 2008.

[4] Nikhil Ganesh and Brian T. Cunningham, "Photonic-crystal near-ultraviolet reflectance filters fabricated," *Applied Physics Letters*, vol. 88, no. 071110, 2006.

[5] S.-T. Wu, Ming Shian Li, and Andy Y.-G. Fuh, "Observation of conical scattering cones from a two-dimensional hexagonal photonic crystal based on a polymer-dispersed liquid crystal," *Optics Letters*, vol. 33, no. 23, pp. 2758-2760, Dec 2008.

[6] F. Yang, G. Yen, and B. T. Cunninham, "Voltage-tuned resonant reflectance optical filter for visible wavelengths fabricated by nanoreplica molding," *Applied Physics Letters*, vol. 90, p. 261109, 2007.

[7] Fuchyi Yang, Gary Yen, and Brian T. Cunningham, "Voltage-tuned resonant reflectance optical filter for visible wavelengths," *Applied Physics Letters*, vol. 90, no. 261109, 2007.

[8] Brian T. Cunningham, "Tunable Photonic Crystal Reflectance Filters on Flexible Plastic Substrates," in *Tri-Service Information Exchange*, 2008.

[9] D. W. Dobbs and B. T. Cunningham, "Optically tunable guided-mode resonance filter," *Applied Optics*, vol. 45, no. 28, pp. 7286-7293, 2006.

[10] M. Auslender and S. Hava, "Zero infrared reflectance anaomaly in doped silicon lamellar gratings. I. From antireflection to total absorption," *Infrared Physics & Technology*, vol. 36, pp. 1077-1088, 1995.

[11] V. G. Kravets, F. Schedin, and A. N. Grigorenko, "Plasmonic blackbody: Almost complete absorption of light in nanostructured metallic coatings," *Physical Review B*, vol. 78, no. 20, p. 205405, 2008.

[12] H. T. Miyazaki et al., "Thermal emission of two-color polarized infrared waves from integrated plasmon cavities," *Applied Physics Letters*, vol. 92, p. 141114, 2008.

[13] Chih-Ming Wang et al., "Reflection and emission properties of an infrared emitter," *Optics Express*, vol. 15, no. 22, October 2007.

[14] F. F. de Medeiros, E. L. Albuquerque, M. S. Vasconcelos, and P. W. Mauriz, "Thermal radiation in quasiperiodic photonic crystals," *Journal of Physics: Condensed Matter*, vol. 19, 2007.

[15] T. S. Luk, T. Mclellan, G. Subramania, J. C. Verley, and I. El-Kady, "Emissivity measurements of 3D photonic crystals," *Photonics and Nanostructures – Fundamentals and Applications*, vol. 6, pp. 81-86, 2008.

[16] I. El-Kady, G. B. Farfan, R. Rammohan, and M. M. Reda Taha, "Photonic crystal high-efficiency multispectral thermal emitters," *Applied Physics Letters*, vol. 93, no. 153501, 2008.

[17] David L. C. Chan, Marin Soljačić, and J. D. Joannopoulos, "Thermal emission and design in 2D-periodic metallic photonic crystal slabs," *Optics Express*, vol. 1419, p. 8785, 2006.

[18] E. L. Dereniak and G. D. Boreman, *Infrared Detectors and Systems*. New York: John Wiley & Sons, Inc., 1996.

[19] Valery Shklover, Leonid Braginsky, Gregoire Witz, Matthew Mishrikey, and Christian Hafner, "High-Temperature Photonic Structures. Thermal BarrierHigh-Temperature Photonic Structures. Thermal Barrier," *Journal of Computational and Theoretical Nanoscience*, vol. 5, no. 5, p. 862–893, 2008.

[20] Thomas A. Germer and Clara C. Asmail, "Goniometric optical scatter instrument for out-of-plane," *Review of Scientific Instruments*, vol. 70, no. 9, 1999.

[21] Shelly A. Uzpen, Michael A. Marciniak, Jeffery W. Burks, and Joseph P. Constantino, "Weathering Effects on Aircraft Paint with Regard to Infrared Signature," US Air Force, 2006.

[22] Bradley Balling, "A Comparative Study of the Bi-Directional Reflectance Distribution Function of Several Surfaces as a Mid-wave Infrared Diffuse Reflectance Standard," Air Force Institute of Technology, Dayton, OH, Thesis 2009.

[23] Eugene Hecht, *Optics*, 4th ed. San Francisco: Addison Wesley, 2002.

[24] Brian Cunningham, Personal Interview, September 2008.

[25] Brian P. Sandford and David C. Robertson, "Infrared Reflectance Properties of Aircraft Paints," Phillips Laboratory, Geophysics Directorate/GPOA, Hanscom, AFB, ESC-94-1004, 1985.

REPORT DOCUMENTATION PAGE

Form Approved
OMB No. 0704-0188

1. REPORT DATE *(DD-MM-YYYY)*	2. REPORT TYPE	3. DATES COVERED *(From - To)*
27-03-2009	Master's Thesis	Apr 2008 - Mar 2009

4. TITLE AND SUBTITLE

Analysis and Application of the Bi-directional Scatter Distribution Function of Photonic Crystals

5a. CONTRACT NUMBER
N/A

5b. GRANT NUMBER
N/A

5c. PROGRAM ELEMENT NUMBER
N/A

6. AUTHOR(S)
Lamott, Robert, B., Capt, USAF

5d. PROJECT NUMBER
N/A

5e. TASK NUMBER
N/A

5f. WORK UNIT NUMBER
N/A

7. PERFORMING ORGANIZATION NAME(S) AND ADDRESS(ES)
Air Force Institute of Technology
Graduate School of Engineering and Management (AFIT/EN)
2950 Hobson Way
WPAFB OH 45433-7765

8. PERFORMING ORGANIZATION REPORT NUMBER
AFIT/GEO/ENP/09-M01

9. SPONSORING/MONITORING AGENCY NAME(S) AND ADDRESS(ES)
Intentionally Left Blank

10. SPONSOR/MONITOR'S ACRONYM(S)

11. SPONSOR/MONITOR'S REPORT NUMBER(S)

12. DISTRIBUTION/AVAILABILITY STATEMENT
DISTRIBUTION A: APPROVED FOR PUBLIC RELEASE; DISTRIBUTION UNLIMITED

13. SUPPLEMENTARY NOTES

14. ABSTRACT

Photonic crystals (PCs) are periodic structures built from materials with different refractive indices repeated at sub-wavelength intervals, which results in unusual optical characteristics, including narrow band laser protection, and zero reflectance and high absorption anomalies. Most of the research into the optical properties of PCs has concentrated only on the small range of wavelengths and angles where these effects occur. To better understand where all light leaving a PC is scattered, a Complete Angle Scatter Instrument was used to analyze the scatter from three Guided Mode Resonance Filters designed for laser protection. In the plane of incidence, measurements of the scatter strength were made for nearly all incident and scattered angles. Reflectance data was also taken out of the plane of incidence for selected incidence angles, showing the directional reflectance over the entire hemisphere. This data was used to modify existing empirically based Bi-directional Scatter Distribution Functions (BSDFs), with the goal of producing a model suitable for scene generation of complex objects coated with a GMRF surface.

15. SUBJECT TERMS
BRDF, BSDF, BTDF, Photonic Crystal, Directional Reflectance, Guided Mode Resonance Filter

16. SECURITY CLASSIFICATION OF:			17. LIMITATION OF ABSTRACT	18. NUMBER OF PAGES	19a. NAME OF RESPONSIBLE PERSON
a. REPORT	b. ABSTRACT	c. THIS PAGE			Michael A. Marciniak, PhD
U	U	U	UU	85	19b. TELEPHONE NUMBER *(Include area code)* michael.marciniak@afit.edu 937-255-3636 x4529

Reset

Standard Form 298 (Rev. 8/98)
Prescribed by ANSI Std. Z39.18